

Stellar populations of massive early-type galaxies observed by MUSE

Taniya Parikh ^{1,2} Roberto Saglia,^{1,3}★ Jens Thomas ^{1,3} Kianusch Mehrgan,^{1,3} Ralf Bender^{1,3} and Claudia Maraston²

¹Max – Planck – Institut für extraterrestrische Physik, Giessenbachstrasse 1, D-85748 Garching bei München, Germany

²Institute of Cosmology, University of Portsmouth, Burnaby Road, Portsmouth PO1 3FX, UK

³Universitäts – Sternwarte München, Fakultät für Physik, Scheinerstrasse 1, D-81679 München, Germany

Accepted 2024 February 9. Received 2024 January 21; in original form 2022 December 6

ABSTRACT

Stellar population studies of massive early-type galaxies (ETGs) suggest that the stellar initial mass function may not be universal. In particular, the centres of ETGs seem to contain an excess of low-mass dwarf stars compared to our own Galaxy. Through high-resolution data from MUSE (Multi Unit Spectroscopic Explorer), we carry out a detailed study of the stellar populations of eight massive ETGs. We use full spectrum fitting to determine ages, element abundances, and initial mass function (IMF) slopes for spatially binned spectra. We measure flat gradients in age and [Mg/Fe] ratio, as well as negative gradients in metallicity and [Na/Fe]. We detect IMF gradients in some galaxies, with the centres hosting bottom-heavy IMFs and mass excess factors between 1.5 and 2.5 compared to a Kroupa IMF. The IMF slope below $0.5 M_{\odot}$ varies for our galaxy sample between 1 and 2.8, with negative radial gradients, while the IMF slope between 0.5 and $1 M_{\odot}$ has a steep value of ~ 3 with mildly positive gradients for most galaxies. For M87, we find excellent agreement with the dynamical mass-to-light ratio (M/L) as a function of radius. For the other galaxies, we find systematically higher M/L from stellar populations compared to orbit-based dynamical analysis of the same data. This discrepancy increases with NaI strength, suggesting a combination of calibration issues of this line and correlated uncertainties.

Key words: galaxies: elliptical and lenticular, cD – galaxies: evolution – galaxies: formation – galaxies: fundamental parameters – galaxies: stellar content.

1 INTRODUCTION

The stellar initial mass function (IMF) is a crucial ingredient in modelling and interpreting the integrated light of galaxies. It regulates star formation and chemical enrichment throughout the life of a galaxy. The IMF was first discovered to be a power law with a slope of $x = 2.35$ (Salpeter 1955) for stars in the Milky Way with masses $>0.5 M_{\odot}$. Later studies revealed a flattening of the power-law slope towards low masses (Kroupa 2001; Chabrier 2003) with a slope of $x = 1.3$ between 0.1 and $0.5 M_{\odot}$ for a Kroupa IMF. In unresolved populations, the IMF can be measured spectroscopically through gravity-sensitive spectral features. The strengths of these features are determined by the ratio of dwarf to giant stars that are present in the stellar population. Alternative methods include constraining the M/L dynamically or through gravitational lensing, and comparing this to the expected M/L for a Kroupa IMF. This ratio of mass-to-light ratios can be thought of as an excess in mass. For massive early-type galaxies, the mass excess was found to increase with velocity dispersion (Thomas et al. 2011b; Cappellari et al. 2012; Conroy & van Dokkum 2012b; Li et al. 2017), and towards the centres of galaxies (Martín-Navarro et al. 2015a; van Dokkum et al. 2017;

Parikh et al. 2018; Domínguez Sánchez et al. 2019; La Barbera et al. 2019; Gu et al. 2022) (see Smith 2020 for a recent review).

Investigations into the reason behind IMF variations have revealed correlations with the velocity dispersion, α -abundance, metallicity, orbital properties (Martín-Navarro et al. 2015b; van Dokkum et al. 2017; Parikh et al. 2018; Poci et al. 2022). Variation has also been observed with kinematics, such that fast rotators (FRs) display bottom-heavy IMFs with steeper radial gradients than slow rotators (SRs) (Bernardi et al. 2019). Combining photometric and kinematic analyses, SRs are cored with a flat central luminosity profile, whereas FRs are cuspy or power-law galaxies, with an extra central component (Kormendy et al. 2009; Emsellem et al. 2011; Lauer 2012). Cored galaxies are thought to be the result of dissipationless (dry) mergers of cuspy galaxies, suggesting that steep IMF gradients become shallower as a result of merging.

The emerging consensus of a varying IMF is still under tension with the results from four strongly lensed galaxies by $2-3\sigma$ (Newman et al. 2017; Collier, Smith & Lucey 2018). Constraints depend on the assumed shape of the IMF, and varying the low-mass cutoff or a non-parametric IMF with free contributions of stars in different mass intervals provides consistent results from lensing and stellar population analysis for all but one of these galaxies. Simulations can also provide insight into this tension as they can be used to study the physical cause of potential IMF variations. Barber, Schaye & Crain (2019) showed using Evolution and Assembly

* E-mail: saglia@mpe.mpg.de

Table 1. Galaxy properties for the sample studied in this work. σ is the velocity dispersion measured from the central radial bin, the half-light radius R_e is taken from literatures (references given in the text), the PSF FWHM is measured from the broadening of point sources in the object or sky exposures, and redshift z is adopted from HyperLEDA.

Galaxy	σ (km s ⁻¹)	R_e (arcmin)	PSF (arcmin)	z
M87	312	81.20	1.20	0.004 28
NGC 1407	261	70.33	1.93	0.005 93
NGC 1332	296	28.00	2.12	0.005 08
NGC 5419	314	43.36	1.56	0.013 76
NGC 5328	318	22.24	1.28	0.015 81
NGC 5516	280	22.09	2.00	0.014 88
NGC 307	183	16.45	2.10	0.013 38
NGC 7619	294	32.00	2.00	0.012 55

of GaLaxies and their Environments (EAGLE) simulations that a pressure dependent low-mass or high-mass IMF slope, calibrated to reproduce the mass excess-velocity dispersion relation in Cappellari et al. (2013), predicts local IMF variations with radius and metallicity as seen in observations. Contrary to this, no departures from a Kroupa IMF have been observed within our own Galaxy, even in the metal-rich bulge which provides environments closer to that of early-type galaxies. Simulations cannot simultaneously explain the IMF variations observed in massive early-type galaxies and the universality of the IMF seen in our own Galaxy (Guszejnov, Hopkins & Graus 2019).

Comparisons of dynamical and stellar population mass-to-light ratios on a galaxy-by-galaxy basis play an important role in assessing any possible systematics. Smith (2014) found no correlation between M/L derived by the two methods, however the dynamical results (Cappellari et al. 2013) were based on a much larger aperture size than stellar populations (Conroy & van Dokkum 2012b). Lyubenova et al. (2016) showed consistency for a subsample of their galaxies when combining constraints from stellar populations and dynamics and when using the same data set over the same apertures. Hence it is crucial to consider radial gradients in the IMF, while noting that these cannot explain cases where the dynamical M/L is higher than the stellar population one. Dynamical studies assuming a constant M/L can affect the mass excess factor by ~ 0.25 dex (Bernardi et al. 2018). Of the few studies which allow a varying M/L , gradients have always been found (Collett et al. 2018; Oldham & Auger 2018). Looking at M87, Sarzi et al. (2018) obtain stellar population-based M/L systematically larger by 30 per cent than those from dynamics (Oldham & Auger 2018), although gradients agree well. Domínguez Sánchez et al. (2019) show agreement between the two methods based on a self-consistent comparison of galaxies from the Mapping Nearby Galaxies at Apache Point Observatory (MaNGA) survey.

In Parikh et al. (2018, hereafter P18), over 300 galaxies from the MaNGA survey were analysed and IMF radial gradients were found for the more massive galaxies in the sample, with Salpeter-like IMFs in the centre, returning to a Kroupa IMF at $1 R_e$. Although these radial gradients were independent of the stellar population model used, the value of the IMF slope between 0.1 and $0.5 M_\odot$ in the more massive galaxy centres, for example, varied from 2 to 3 depending on the model. Discrepancies also exist depending on the region of the spectrum being fit. Conroy & van Dokkum (2012b) show using their models that masking the NaI region strongly influences the resulting IMF slope despite carrying out full spectrum fitting. Martín-Navarro et al. (2021) apply a hybrid *full index fitting* approach, that fits each pixel within the bandpass of chosen indices, with TiO

indices as the IMF-sensitive features. It would be interesting to see the derived [Ti/Fe] values in order to assess residual degeneracies affecting these indices. Sarzi et al. (2018) derive similar IMF gradients using different combinations of indices (e.g. TiO, NaI, CaT) using Vazdekis et al. (2012) models. In addition to the choice of stellar population models and fitting technique, uncertainties can arise due to the underlying stellar library being incomplete. New stellar libraries such as Yan et al. (2018; MaStar) and Verro et al. (2022; X-shooter Spectral Library) will help shed further light on this matter.

In this work, we build upon previous studies in three aspects: (i) we model individual massive galaxies in detail with increased spatial resolution thanks to Multi-Unit Spectrograph Explorer (MUSE), generating maps of stellar population properties for these galaxies, (ii) the sample contains galaxies with different kinematic morphologies to explore in detail trends between slow versus fast rotators and their IMF, and (iii) we compare the M/L from stellar populations with the independently derived dynamical M/L from literature to provide strong constraints. We aim to use a galaxy-by-galaxy approach to assess the consistency between these two techniques, and also attempt to investigate variations with kinematics to shed further light on the driver of IMF variations.

In Section 2, we describe our MUSE galaxy sample and binning procedure. Section 3 presents our derived stellar population parameters for all the galaxies including spatial maps. We compare our M/L profiles to dynamical modelling results in Section 4 and discuss the implications, with our concluding remarks in Section 5.

2 DATA

2.1 Galaxy sample

We use data from the European Southern Observatory (ESO) programme 095.B-0624(A) (PI: Jens Thomas) for early-type galaxies observed by MUSE mounted on the 8.4m UT4 of the Very Large Telescope. Of these, NGC 6861 and NGC 4751 are excluded from the present analysis due to poor quality data in the near-infrared, which is crucial for IMF derivation. We also use MUSE observations of M87 (Sarzi et al. 2018), giving a sample of eight galaxies with a median redshift of 0.013. The observations are in the wide-field mode, with a wavelength coverage of 4800–9400 Å and a spectral resolution of 1.25 Å (see Mehrgan et al. 2023b for more details on the observations). NGC 307 and NGC 1332 are fast rotators, while the others are intermediate/slow rotating galaxies.

The properties of these galaxies are listed in Table 1. σ is the maximum central velocity dispersion as measured in this work, R_e comes from previous publications: M87 from Gebhardt & Thomas (2009); NGC 1407, NGC 5328, NGC 5516, and NGC 7619 from Rusli et al. (2013); NGC 1332 from Rusli et al. (2011); NGC 307 from Erwin et al. (2018); NGC 5419 from Mazzalay et al. (2016). The full width at half-maximum (FWHM) of the point spread function (PSF) is measured from the broadening of point sources in the object or sky exposures, while redshifts are adopted from Hyper-Linked Extragalactic Databases and Archives (HyperLEDA).

Of the galaxies in our sample, M87 (Sarzi et al. 2018) and NGC 1407 (van Dokkum et al. 2017) have been previously analysed and found to contain steep IMF gradients. The prior is analysed using indices and Vazdekis et al. (2012) models and the latter using full spectrum fitting with Conroy models (same as our approach). However the data for the latter is different. We provide a detailed comparison of our results with these works in the Results section.

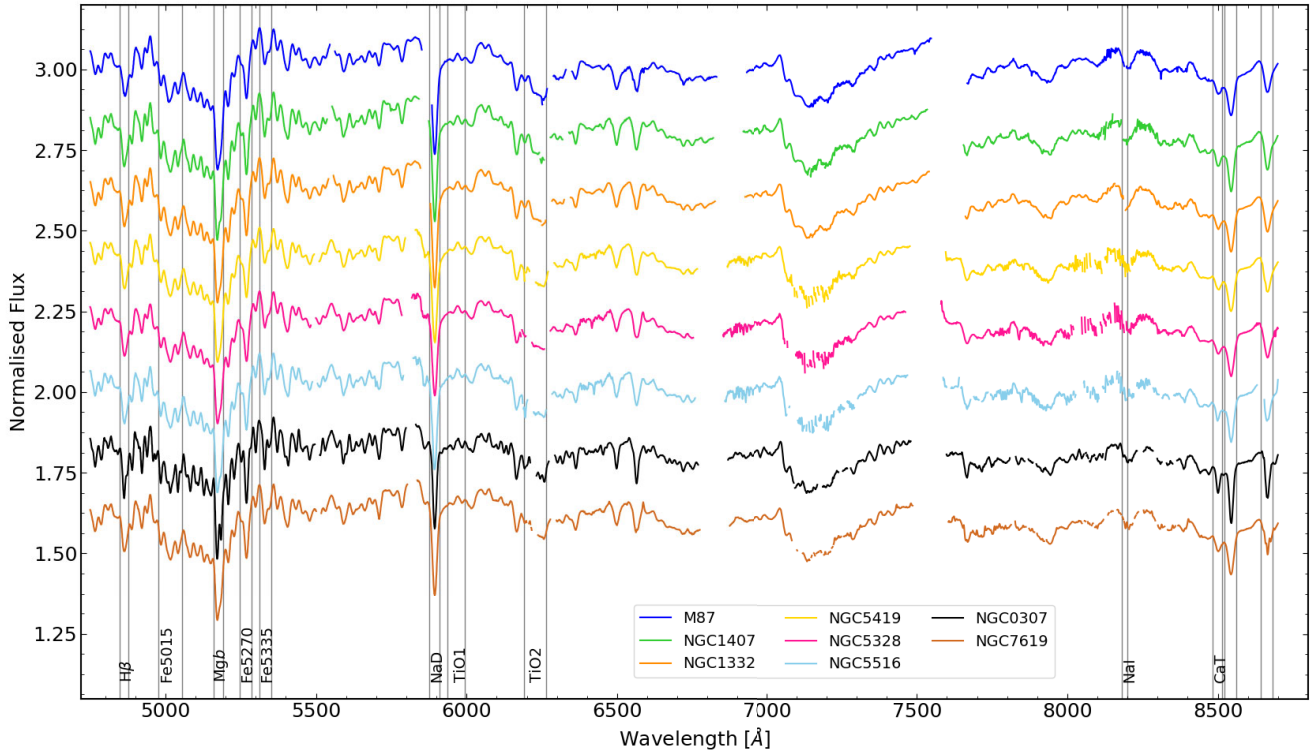


Figure 1. The central radially binned spectrum of each galaxy is shown in the rest frame. Key absorption features are labelled and masked regions (due to sky and telluric residuals) are omitted.

2.2 Spectra

We proceed to stack galaxy spectra in elliptical annuli for all galaxies, and also in Voronoi bins for galaxies with higher signal-to-noise ratio (S/N) in order to achieve more spatial resolution in these cases. The elliptical annuli are along the semimajor axis and the number of bins are chosen depending on the effective radius coverage within the MUSE field of view (FOV), while the Voronoi bins have a target S/N of ~ 400 . Foreground stars and other galaxies in the FOV are masked and individual pixels with $S/N < 5$ are excluded from the binning. There are two sources of error in a binned spectrum: the observational error associated with the data (which includes errors due to sky subtraction), and the error on the mean due to the standard deviation of all spectra within a bin. We combine these in quadrature to derive the error spectrum.

Binned spectra are fit using PPXF (Cappellari 2017) to determine stellar kinematics and to subtract emission lines where present. We remove emission associated with $H\beta$, $[O\text{ III}] \lambda 4960$, $\lambda 5008$, $[N\text{ I}] \lambda 5199$, $\lambda 5202$, He I, $[O\text{ I}] \lambda 6302$, $\lambda 6366$, $H\alpha$, $[N\text{ II}] \lambda 6550$, $\lambda 6585$, $[S\text{ II}] \lambda 6718$, $\lambda 6733$. We impose a limit that the $[N\text{ I}]$ line, just redward of Mgb , is only subtracted when the emission strength-to-error ratio is greater than 10, since the routine tries to fit something even when no emission is present. This led to $[N\text{ I}]$ emission being fit only for inner bins, as expected. Spectra are then shifted to rest frame using the redshift and rotation velocity. For the radial bins, spectra are shifted to rest frame using the velocity from the Voronoi bins before binning. This greatly improves the spectral quality in the near-infrared for the fast rotators, since the high-stellar rotation velocity means that the sky residuals are shifted to slightly different wavelengths and are reduced when averaging spectra together. We

mask out three strong sky line regions (5270–5586, 6295–6315, 6357–6377; observed frame wavelengths), two deep telluric regions (6860–6960, 7580–7700 Å), and NaD absorption from the Milky Way (5570–5586 Å).

Central binned spectra for all galaxies are shown in Fig. 1. Sky lines and regions with strong telluric residuals are masked and the wavelengths are in the rest frame. NGC 5516, NGC 5419, and NGC 5328 are all in particular affected in the NaI region near 8200 Å, due to their redshifts. For M87, the central 3 arcmin and the jet of material from the active galactic nuclei are masked, since the continuum is contaminated by synchrotron emission in these regions.

2.3 Stellar population models

For these massive galaxies we require stellar population models at high metallicities, along with a large grid of IMFs and element abundances. For this purpose the models of Conroy et al. (2018) are presently the most suitable, based on the stellar library described in Villaume et al. (2017) and theoretical response functions for various elements. The stars come from Medium resolution INT Library of Empirical Spectra (MILES) and extended Infrared Telescope Facility (IRTF) libraries providing supersolar metallicity coverage, topped up with dwarf stars from Mann et al. (2015) to cover the cool dwarf regime.

Fitting the full spectrum or fitting absorption strengths are complementary approaches for deriving stellar population parameters. While full spectrum fitting makes use of all available information and leads to smaller errors compared to fitting indices for spectra of the same S/N (Conroy et al. 2018), indices exploit key information encoded within narrow wavelength regions, avoiding regions of

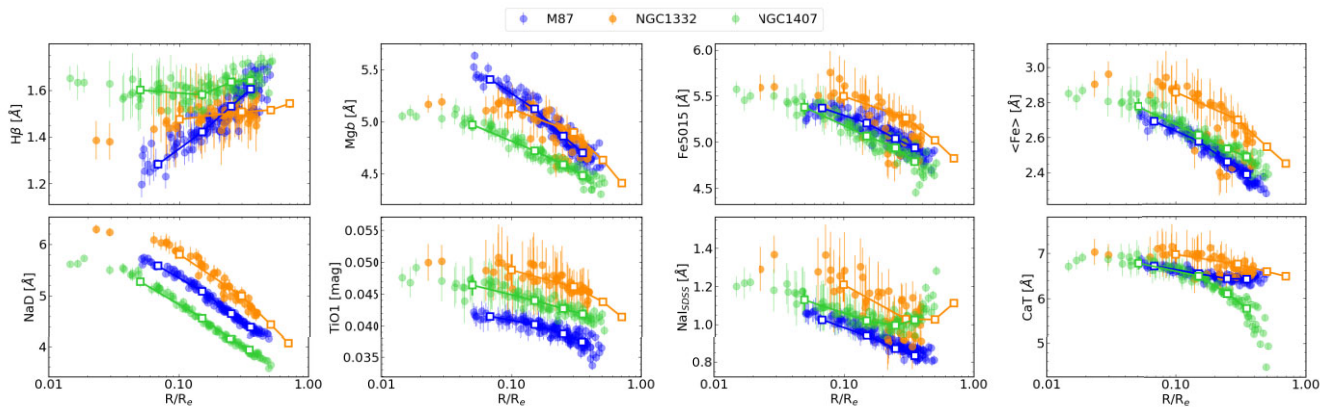


Figure 2. Key absorption line strengths are shown as a function of radius for the three galaxies studied in greater detail. Filled symbols are measurements on the Voronoi binned spectra, while open symbols are measured on the elliptical annuli. The two binning schemes provide consistent results. All indices show negative radial gradients except for $H\beta$, which is flat or increases mildly with radius. NaD shows a particularly steep rise towards the centre.

the spectrum which are noisy or not well understood. We measure absorption strengths using equations (2) and (3) from Worthey et al. (1994), with the optical index definitions from Trager et al. (1998), NaI_{SDSS} from La Barbera et al. (2013), and CaT from Conroy & van Dokkum (2012a). The measurements are corrected to a common resolution using correction factors calculated from the Maraston et al. (2020) stellar population models. To do this, we measure the indices on the models at two dispersions: the σ of the galaxy bin as derived from PPXF, and at 250 km s^{-1} . We use the ratio between these as a correction factor to obtain indices at 250 km s^{-1} resolution.

We make use of the full spectrum fitting code ALF (Conroy & van Dokkum 2012a; Conroy et al. 2018) which explores up to 42 parameters with Markov chain Monte Carlo (MCMC). Compared to the van Dokkum et al. (2017) setup, we have the following differences: we allow the higher order Gauss–Hermite moments, $h3$ and $h4$, to vary; the element abundances Cu/H and Eu/H are also kept free; the low-mass cutoff of the IMF is fixed to 0.08. Unfortunately we are unable to vary the latter since these models are not publicly available. We tested keeping the other parameters fixed and found no significant effect on our results. We show the Gauss–Hermite parameters in section C and plan to implement a fully non-parametric line-of-sight velocity distribution (LOSVD) as an input to the full spectrum fitting code in the future, motivated by the results of Mehrgan et al. (2023b).

The IMF slope can be varied in two regions: between 0.08 and $0.5 M_{\odot}$ and 0.5 and $1 M_{\odot}$, referred to as X1 and X2, respectively. We split the fit into four regions: 4750–5750, 5750–6750, 6750–7750, and 7750–8700 Å, such that within each region the continuum is normalized via a polynomial with one order per 100 \AA . Thus the fits begin close to the blue limit for MUSE, and end just after the CaT triplet, since spectra red-ward of this are too noisy to provide any useful information. For these models and code, the metallicity is quoted as $[\text{Fe}/\text{H}]$. We convert this to total metallicity $[\text{Z}/\text{H}]$ using equation (13) in Johansson, Thomas & Maraston (2012).

2.4 Residual telluric absorption

The telluric correction, calculated using a standard star as described in Mehrgan et al. (2023b), has an associated statistical error. We carried out an exercise to estimate errors due to the uncertainties in the telluric correction. We produced five mocks for NGC 1407 by

perturbing the spectrum using this error. Calculating the root mean squared difference for all parameters between each mock and the results presented in this work showed that the effect on the IMF slope X1, and M/L, was significantly large. $[\text{Z}/\text{H}]$ was also affected, but for all other parameters the rms was comparable to or smaller than the errors derived by ALF. We add this uncertainty in quadrature to the error estimates from ALF.

3 RESULTS

In this section we present the results of our analysis, starting with the absorption strengths, followed by the derived stellar population parameters. For the absorption strengths, we first show the Voronoi binned data and overlay the radial data for the three galaxies with detailed analyses, followed by the radial results for all eight galaxies. This allows us to demonstrate consistency between the two binning techniques, i.e. Voronoi and elliptical annuli, and present detailed results where available.

3.1 Index measurements

Fig. 2 shows measurements of key indices as a function of radius for the three galaxies studied in greater detail. The measurements have been corrected to 100 km s^{-1} (the resolution of the stellar population models) and $1 - \sigma$ errors are shown. Filled symbols represent measurements from the Voronoi bins, and open symbols are results from the elliptical annuli. These binning methods appear consistent with each other, providing confidence in the other galaxies with just radial binning.

Massive galaxies are known to have stronger metallic indices and weaker $H\beta$ (Bender, Burstein & Faber 1992; Trager et al. 1998), as we also see here. All indices display negative radial gradients except for $H\beta$, which is either flat or positive (in the case of M87). This is an age-sensitive index and a positive gradient indicates slightly younger stellar populations in galaxy outskirts. M87 shows relatively strong Mg b absorption and weaker Fe indices, which is important because the combination of these indices sets $[\text{Mg}/\text{Fe}]$ and provides an indication of star-formation time-scales. Looking at NaD, all galaxies show strong absorption, which steepens considerably towards the centres, this is linked to highly enhanced $[\text{Na}/\text{Fe}]$ found in centres of massive early-type galaxies. These intrinsic

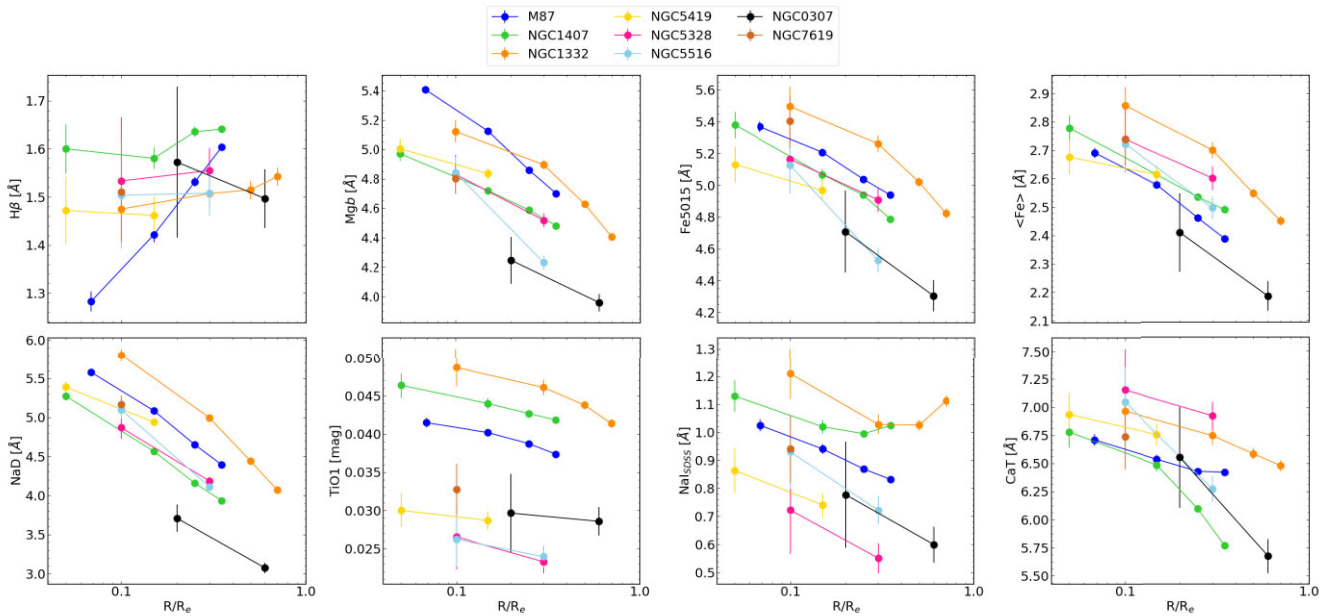


Figure 3. Same as Fig. 2 measured on the elliptical annuli bins for the full sample of galaxies. All galaxies have high velocity dispersions; NGC 307 which has lower σ is shown in black. $H\beta$ falling towards the centre for M87 is likely caused by residual emission. M87 also has very strong Mgb absorption, and relatively weaker $\langle Fe \rangle$. NGC 1332, NGC 1407, and M87 have the strongest IMF-sensitive indices TiO1 and NaI. Generally galaxies with stronger TiO and NaI display weaker CaT, and vice versa (with the exception of NGC 1332).

differences in the spectra indicate the presence of different stellar populations.

The IMF sensitive NaI index is also very strong in galaxy centres with values between 1 and 1.4 Å. NGC 1332 and NGC 1407 appear to rise at larger radii, which is likely as a result of systematics due to residual sky and tellurics. Note that the annuli for NGC 1332 cover larger radii than the Voronoi bins because shifting spectra before binning helps reduce sky and telluric residuals. High rotation velocities in this galaxy lead to these residuals being shifted to different wavelengths, which are therefore reduced when averaging. The rising NaI at large radii in both the NGC 1407 Voronoi bins and the NGC 1332 radial bins suggests that the data might not entirely be reliable in the near-infrared (NIR). These pixels are masked during the full spectrum fitting and hence do not affect the derived parameters.

Next, Fig. 3 shows the same equivalent widths for radial bins for the full sample of galaxies. For NGC 7619, we are only able to analyse a single binned spectrum out to $0.2 R_e$. The clear positive $H\beta$ gradient in M87 is seen here, but central values could be underestimated due to poorly subtracted emission. Since this is the only galaxy with emission, the positive gradient is unlikely to be physical and suggests that the emission lines in M87 are not well modelled. We test our full spectrum fitting results when $H\beta$ is masked and find little to no effect on the age and other parameters, suggesting that the fitting is robust to emission residuals. Looking at the IMF sensitive indices it is important to note that NGC 1332, NGC 1407, and M87 present both strong NaI and strong TiO absorption. NGC 307 has the lowest dispersion which leads to weaker index strengths e.g. Mgb , $\langle Fe \rangle$, NaD relative to the other galaxies, but note that it has relatively high NaI line-strengths with central values reaching 0.8 Å.

There appears to be an anticorrelation between TiO1 and NaI index strengths with CaT, while noting that NGC 1332 does not follow this pattern. It is also interesting to see that while e.g. NaD shows larger

local (within the galaxy) gradients than across the sample of galaxies, TiO1 shows much larger global (across galaxies) variation compared to its mild local gradients.

3.2 Full spectrum fitting

The fits from the full spectrum fitting code are shown for M87 in Fig. 4 for a radial bin from the centre within $0.1 R_e$ and near $0.5 R_e$. These data are shown in black and purple, respectively, and the best-fitting model in red. Grey boxes highlight regions masked due to sky and telluric residuals. The fits to the data are high quality, well within the error at most wavelengths with residuals <0.5 per cent.

The spectrum from larger radii shows issues with sky and telluric residuals in the near-infrared. We mask additional regions due to sky and telluric residuals using a threshold when the sky or telluric signal compared to the flux is >5 percent. This limit provided a means to mask a majority of the large spikes seen in the spectra while also ensuring not too much of the data is excluded. Naturally there are more masked pixels in outer bins as the signal from the galaxy decreases. We tested applying the maximum mask from the outermost bin to all spectra and the results were not affected. Prior to this, we discard some outer radial bins with too many masked pixels in the NIR, for all galaxies except M87, NGC 1407, and NGC 1332. Appendix A shows the fits to the other galaxies for the central and outer radial bins.

3.3 Stellar population parameters

Fig. 5 shows spatial maps of the stellar population parameters for M87 in the entire MUSE FOV, which goes out to $0.5 R_e$. The age is uniformly old between 13 and 14 Gyr (note that the full spectrum fitting code has a prior on the age parameter, restricting its value to younger than the age of the universe), despite the positive $H\beta$ index

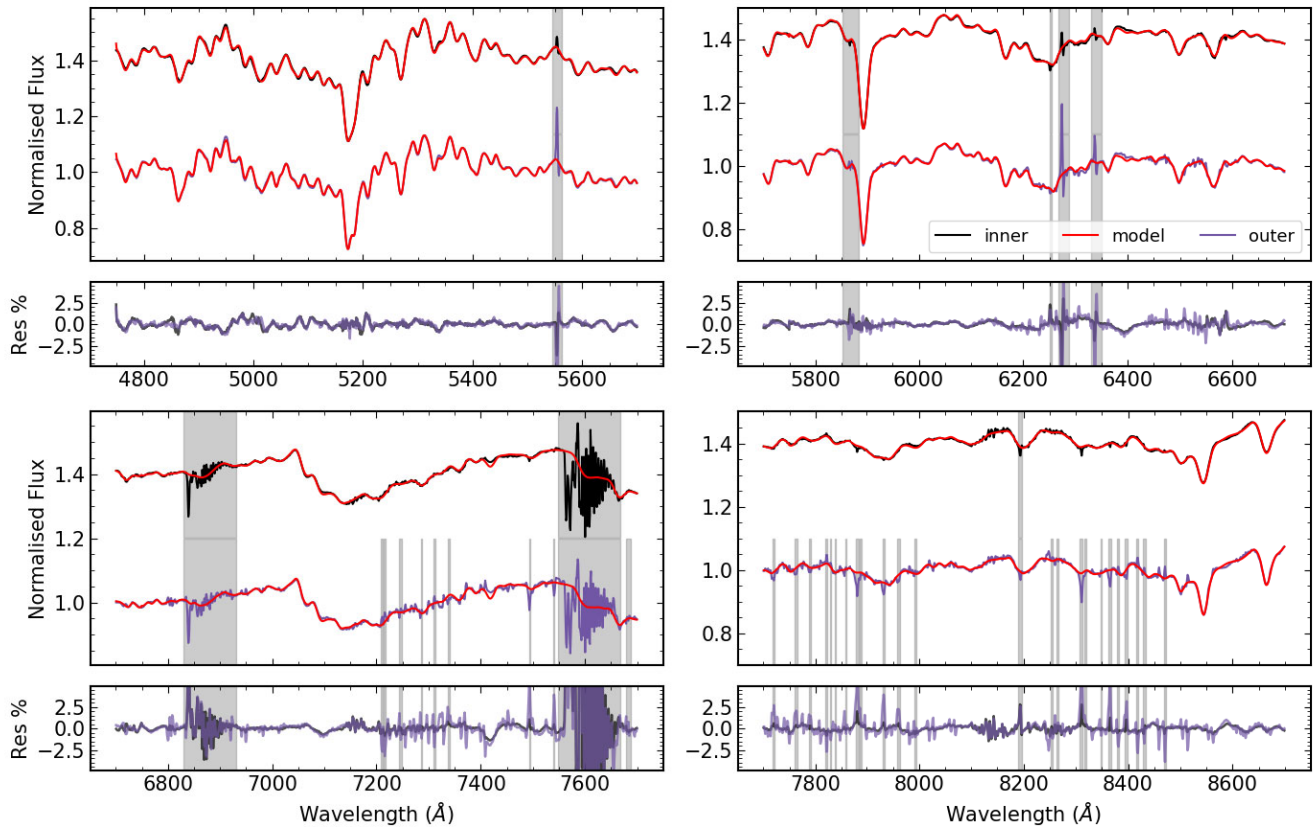


Figure 4. The best-fitting stellar population models (red) to binned M87 spectra are shown for the central bin (black) and an outer bin at $0.5 R_e$ (purple). The spectra have been offset for clarity. Masked regions due to strong sky and telluric residuals are highlighted in grey. The residuals are generally below 0.5 per cent in the centre and ~ 1 per cent at larger radius.

gradient, which is likely affected by emission. Hence, full spectrum fitting circumvents this issue. There are signs of slightly younger stellar populations at larger radii, however this needs to be studied out to larger distances than probed in this work. There is a metallicity gradient with twice-solar metallicities in the centre, falling to 0.1 dex at $0.5 R_e$. These age and metallicity profiles are as expected for early-type galaxies.

Moving on to the element abundances, $[\text{Mg}/\text{Fe}]$ and $[\text{Ca}/\text{Fe}]$ are uniform with values of 0.40, 0.05 dex, respectively. These trends are consistent with literature such that Mg is enhanced to twice-solar values, while Ca is relatively under-abundant. Mild gradients are seen in N: $[\text{N}/\text{Fe}]$ has central values of 0.25 dex decreasing to ~ 0.1 dex moving outwards. $[\text{Na}/\text{Fe}]$ is the most enhanced with central values of 0.6 dex and displays a steep gradient, falling to 0.4 dex/ R_e near the outskirts. The lower mass IMF slope, X1 has a shallow negative gradient, while X2 has large values of ~ 3 at all radii. Lastly, the mass excess factor, α_{Kroupa} has a mild gradient from 1.5 in the centre to 1 at larger radii. The mass excess factor is the best-fitting M/L divided by the expected M/L for a Kroupa IMF.

The parameters from Fig. 5 plus dispersion and additional elements C, Ti, are now shown as a function of radius in Fig. 6 for the elliptical annuli bins of the full sample of galaxies. All galaxies display old stellar populations with slightly younger ages at large radii. Metallicity gradients, where present, are negative; NGC 5419, NGC 5516, and NGC 307 appear to be very metal-rich >0.3 dex out to the radius we are able to study.

Interesting results are seen for different element abundances. $[\text{Mg}/\text{Fe}]$ values are tightly constrained around 0.3 dex for all galaxies at all radii. M87 however has higher values of 0.4 dex and combined with old ages, this means that these stellar populations formed very early on and quickly. $[\text{C}/\text{Fe}]$ values are contained within 0.20–0.25 dex, with no gradients, while $[\text{Ti}/\text{Fe}]$ shows a larger spread of values between solar and twice-solar, again with no significant gradients. $[\text{N}/\text{Fe}]$ has similar values with negative gradients. $[\text{Ca}/\text{Fe}]$ values are between solar and 0.1 dex, as previously found for massive early-type galaxies (Saglia et al. 2002; Cenarro et al. 2003). Lastly, $[\text{Na}/\text{Fe}]$ shows steep radial gradients in all galaxies. These profiles reflect the NaD index strengths measured in Fig. 3.

We are able to compare our results for M87 and NGC 1407 with abundance profiles from literature for some elements. Our results agree with Sarzi et al. (2018) for $[\text{Z}/\text{H}]$ and $[\alpha/\text{Fe}]$ (comparing to our $[\text{Mg}/\text{Fe}]$) in the centre but owing to their steeper gradients, their outer values are smaller at -0.1 and 0.3 dex (compared to our 0.1 and 0.4 dex). They also have steeper $[\text{Na}/\text{Fe}]$ gradients, such that they find a central maximum values of 0.7 dex (compared to our 0.55 dex), while we agree in the outer regions. We find qualitatively consistent results with van Dokkum et al. (2017) for C, Ca, Mg, and Na. A detailed inspection reveals minor differences of the order of 0.05 dex (we find higher central C and Ca and lower Na). The largest difference is that our $[\text{Fe}/\text{H}]$ are offset to lower values. While they report central values of 0.1 dex, falling to -0.25 dex at our radial limit, we find -0.05 dex at the centre with a mild decrease to -0.1 dex. These differences are likely due to a combination of the wavelength ranges

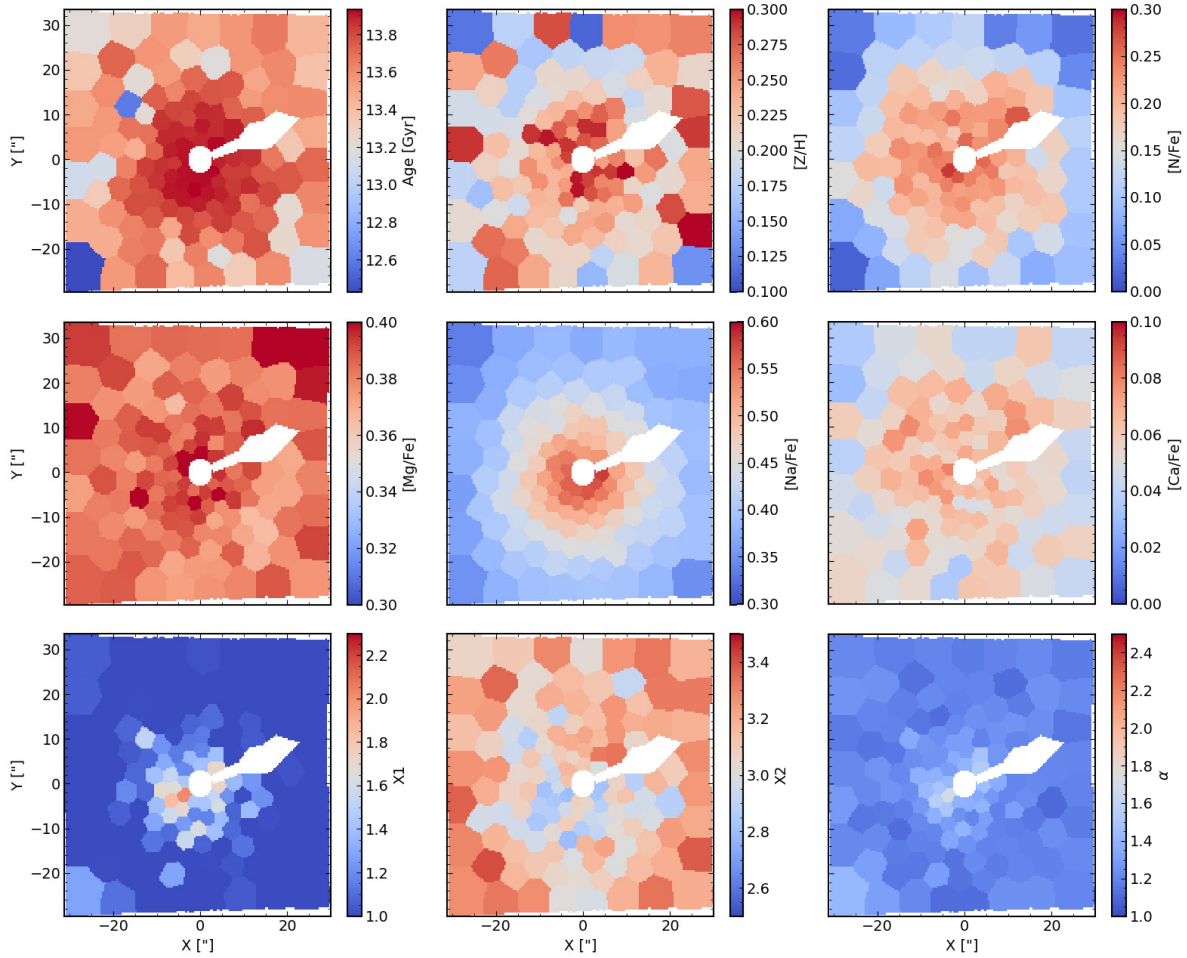


Figure 5. Maps of stellar population parameters derived from full spectrum fitting are shown for M87. The FOV covers the galaxy out to ~ 40 arcsec, which is $0.5 R_e$. The galaxy displays an old stellar population with a negative metallicity gradient. Uniform abundance patterns are seen for Mg and Ca, while N and Na display negative gradients. The IMF slope X1 is found to have a radial gradient from 1.8 in the galaxy centre to below 1 in the outer parts; X2 has larger values ~ 3 , leading to a mass excess of ~ 1.5 compared to Kroupa.

used in all the studies and the different stellar population models in Sarzi et al. (2018). Note that although both works are based on the same observations, differences can arise due to the method of sky and telluric correction in the data reduction pipelines.

Parikh et al. (2021) found negative gradients for [Na/Fe], while the other five elements were uniform with radius for early-type galaxies. All elements showed clear trends with mass or velocity dispersion. We include a detailed discussion of our element abundances in Section 4.1 and compare with literature values, particularly Parikh et al. (2021).

The final three panels show the IMF slopes X1, X2, and the best-fitting M/L ratio in the V band. X2, the IMF slope between 0.5 and $1.0 M_\odot$ has a value of ~ 2.3 for both Kroupa and Salpeter IMFs, as indicated by the dashed line. In the panel for X1, the slope between 0.08 – $0.5 M_\odot$, dashed lines indicate Kroupa and Salpeter IMFs. X1 shows much more variation across galaxy centres and within galaxies, and mostly negative gradients. X2 has values of ~ 3 at all radii and appears to be more tightly constrained with smaller error-bars. van Dokkum et al. (2017) also find negative radial gradients in X1, with values of ~ 3.0 in the centre to 1.5 at larger

radii. Instead for X2, they find values of ~ 2.1 , with a mild increase to 2.4 for the outermost bins.

X1 and X2 appear to be anticorrelated and NGC 5419 is the most extreme example. An anticorrelation between the IMF slopes has also been found by Feldmeier-Krause, Lonoce & Freedman (2020), for the galaxy NGC 3923. Note that the parameters derived by van Dokkum et al. (2017) do not show this. Therefore all galaxies have an enhanced fraction of dwarfs between 0.5 and $1 M_\odot$; M87, NGC 5328, and NGC 307 have gradients in X1 ranging from between Kroupa and Salpeter in the centre to below Kroupa at larger radii, NGC 5419 and NGC 7619 display super-Salpeter IMFs, with the other galaxies in between. This is reflected in the stellar M/L in the V band. Also shown as dotted lines in the last panel is the M/L ratio for a Kroupa IMF. Hence, gradients in the dotted lines are due to only the age or metallicity. It is clear that the largest impact on the M/L value and slope is due to the IMF.

Next, Fig. 7 shows the mass excess factor as a function of the velocity dispersion. The galaxies from this work are shown as before and the symbol size indicates radius such that larger circles correspond to galaxy centres. Also shown are the results from P18

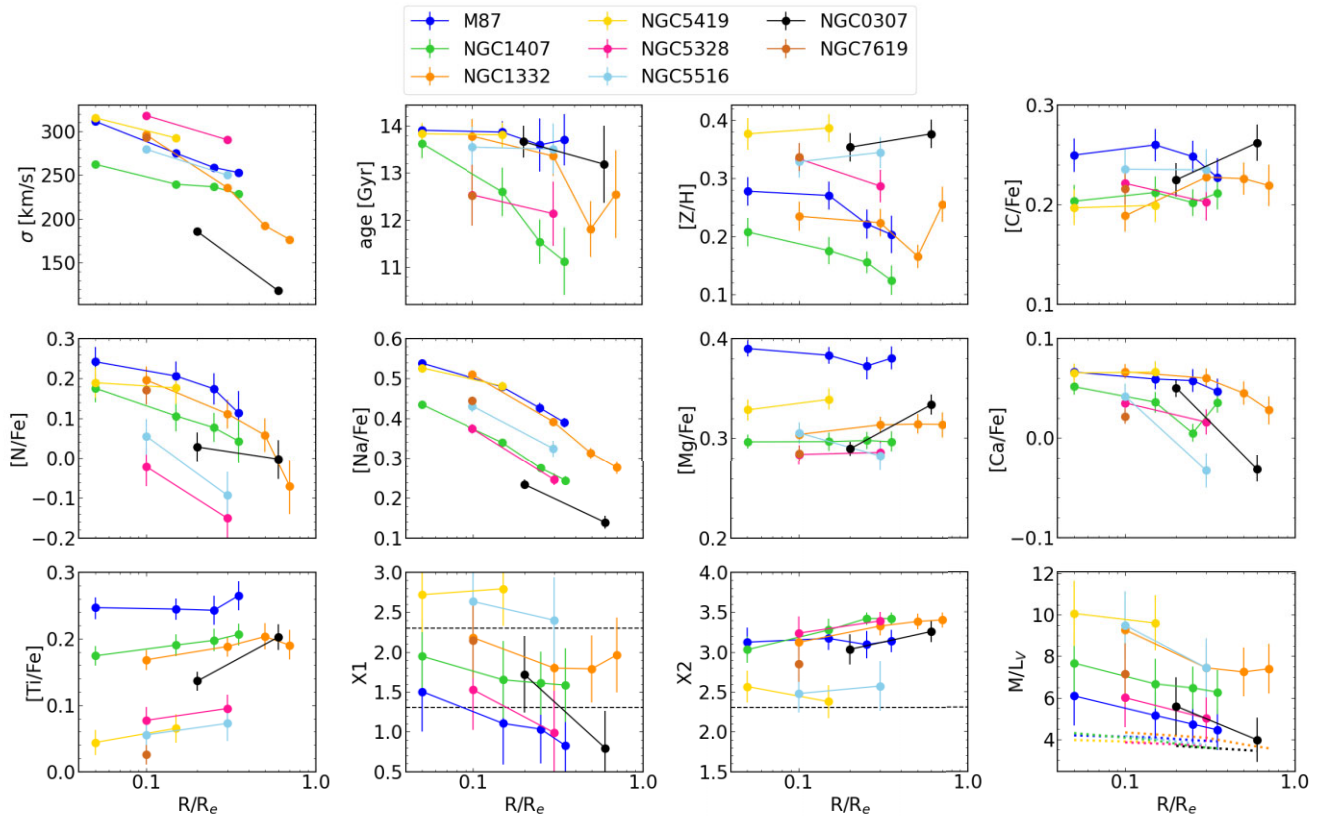


Figure 6. Stellar population parameters as a function of radius for the entire sample of galaxies. There are clear differences between the galaxies: M87 is the most Mg-rich (as well as having high abundances for the other elements). Strong negative gradients in $[\text{Na}/\text{Fe}]$ are found for all galaxies and in the IMF slope X1 for some galaxies. The dashed lines in the IMF slope X1 panel correspond to Salpeter and Kroupa IMFs at 2.3 and 1.3, respectively, and the dashed line for X2 at 2.3 represents both. Finally, the coloured dashed lines in the final panel show M/L when the IMF is fixed to Kroupa.

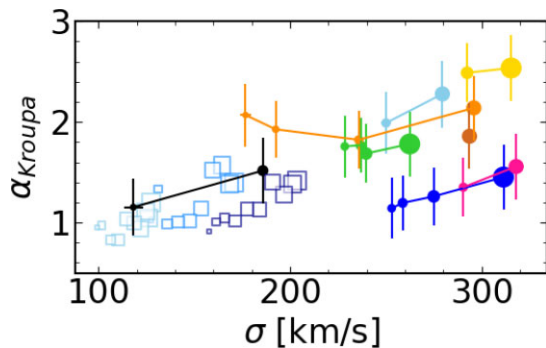


Figure 7. The mass excess factor compared to a Kroupa IMF is shown as a function of the velocity dispersion. Radial bins are shown for each galaxy connected by lines. Also shown for comparison are the results based on MaNGA data from P18 for three mass bins with darker colours representing more massive galaxies. For both data sets, symbol size decreases as radius increases. The present results extend the MaNGA analysis to more massive objects and show that the stellar population models predict an increasingly larger mass excess with increasing σ . M87 and NGC 5328, despite having much larger σ than NGC 307, have a similar mass excess to it.

as open squares. These are three mass bins spanning 9.9–10.8 $\log M/M_{\odot}$, where the higher mass (higher velocity dispersion) bins show a gradient between Salpeter and Kroupa, and the lowest mass bin displays a Kroupa IMF at all radii. This work extends this to higher masses showing that more massive galaxies have even steeper IMFs.

In terms of the gradients, we see a variety such that some galaxies show a gradient while others are bottom-heavy out to our radial coverage. Hence, we find an α – σ correlation but see that individual galaxies show scatter in this relation.

The mass excess factor is between 1 and 2.5 for all galaxy centres. NGC 307 displays the same IMF slope and gradient as slow rotators of much larger velocity dispersions (M87 and NGC 5328). NGC 307 has comparable dispersion to the MaNGA results from P18, and has similar or slightly larger IMF than these. It is important to note that these analyses differ in method (full spectrum fitting versus indices) as well as stellar population models.

We also set out to explore IMF trends with kinematic morphology. Of the two fast rotating galaxies in our sample, NGC 1332 shows a bottom-heavy IMF and large M/L . The other fast-rotator, NGC 307, also shows a steeper IMF relative to its low dispersion. Yet similar variations are seen amongst the slow rotators. Hence, we see some hints that cuspy galaxies might have more bottom-heavy IMFs than cored galaxies on average, however this can only be confirmed with a larger galaxy sample. Bernardi et al. (2019) find that fast rotators have more bottom-heavy IMFs and steeper gradients than slow rotators for a large sample of galaxies from the MaNGA survey.

We explore correlations between stellar population parameters in Fig. 8. The mass excess is plotted against the metallicity and Na abundance. Decreasing symbol size indicates increasing radius, and results from P18 are shown as square symbols, as before. There is scatter compared to the results of the MaNGA data in average mass

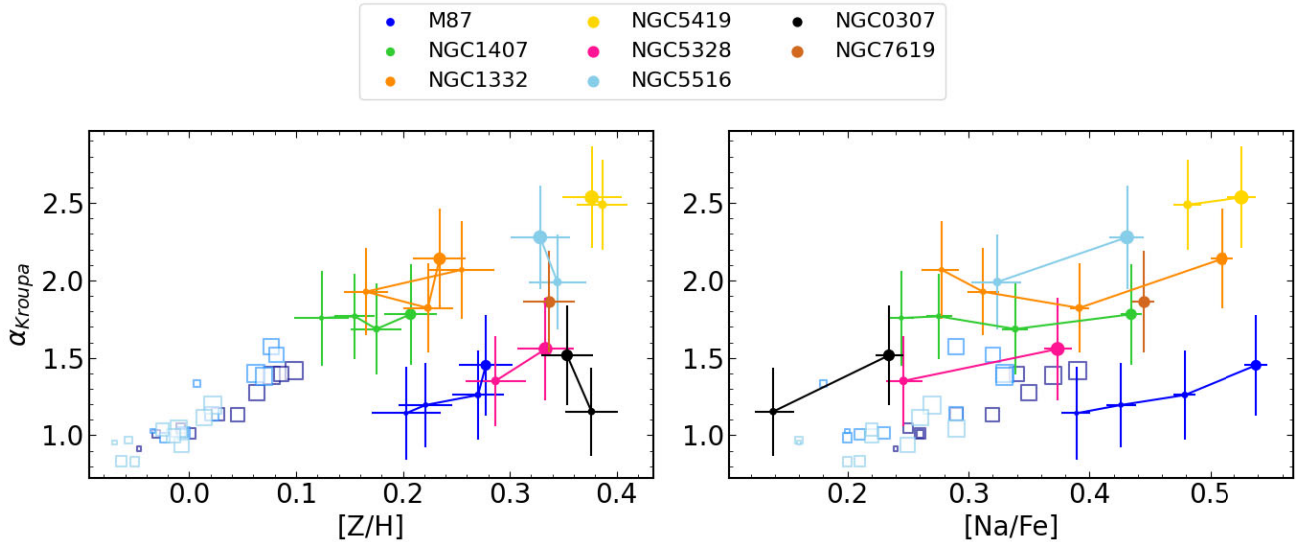


Figure 8. Correlations of the mass excess factor with metallicity (left) and with Na abundance (right) are shown. Symbol colours and sizes as before from Fig. 7. Although results for the individual galaxies lead to more scatter, the correlations found from the MaNGA data appear to hold for more massive galaxies. M87 has very high $[Na/Fe]$ and low $[Z/H]$ for its mass excess.

bins, but the correlation appears to extend when studying higher mass galaxies. M87, NGC 5328, and NGC 307 appear to have less mass excess for their metallicities. M87 also has low mass excess compared to its high $[Na/Fe]$, but for the other two galaxies the lower Na abundance could explain the deviation from the α - $[Z/H]$ relation.

4 DISCUSSION

4.1 Comparison of element abundances

The accuracy of abundances directly affects the IMF slope. For example, if $[Na/Fe]$ is under or overestimated, the NaI index would receive less or more contribution from Na abundance and consequently the IMF would be over or underestimated.

We compare our parameters with the results for early-type galaxies from P21 in Fig. 9. These are based on six mass bins between 8.8 and 11.3 $\log(M/M_{\odot})$ and plot the results out to 1 R_e here. These are shown as open squares, where galaxy mass increases from yellow to red shades. The present analysis is shown for individual galaxies as coloured symbols connected by lines, as in the previous plots. All but NGC 307 are similar mass or more massive than the highest mass bin from P21, which is 11–11.3 $\log(M/M_{\odot})$ and shown in red.

Our ages and metallicities are larger (older and more metal rich) than the MaNGA-based results. We also find shallower gradients in the present analysis. Note that the total metallicity in this work was not derived directly, but calculated using $[Fe/H]$ and other abundances. N, Na, and Mg are also consistent between the two analyses. NGC 5516 and NGC 5328 are outliers with lower $[N/Fe]$ than the other galaxies of similar masses and dispersions by 0.2 dex. Meanwhile C, Ca, and Ti are offset to lower abundances for the current analysis. These differences are likely due to a combination of the choice of stellar population models and the wavelength range of the data. We cannot repeat our present analysis with the Thomas, Maraston & Johansson (2011a) as in P21 since the MUSE data does not cover the bluer wavelengths containing the necessary absorption features. A comprehensive discussion of the treatment of

these elements in the different models and comparison of previous literature results (which show similar offsets as here) is included in Parikh et al. (2019). It remains to be investigated what impact the differences between the abundances of these particular elements might have on the derived IMF slope.

4.2 Comparison with dynamical M/L

We now present a comparison of the M/L derived in this work (always shown in blue) with literature results from stellar populations and dynamics-based analyses, where available. All M/L are reported in the V band. We start with M87 in Fig. 10, which has been analysed a lot in literature. NGC 1407 and NGC 1332 are shown in Fig. 11 and the remaining four galaxies are shown in Fig. 12. NGC 7619, for which we analysed a single global spectrum, is discussed in the text. Literature results are labelled D for dynamics or SP for stellar populations. Shaded regions and error bars represent $1 - \sigma$ errors. The shaded region from Sarzi et al. (2018) includes systematics due to different methods used to infer the IMF.

For all galaxies except M87, Spectrograph for INtegral Field Observations in the Near Infrared (SINFONI) kinematics with high spatial resolution are available and all these galaxies have advanced orbit-based dynamical models that include a central supermassive black hole, stars, and a dark-matter halo (Mehrgan et al. 2023a; Neureiter et al. 2023b).

The combination of MUSE and SINFONI together with a novel model selection technique allowed for highly accurate mass determinations (Lipka & Thomas 2021; de Nicola et al. 2022; Thomas & Lipka 2022; Neureiter et al. 2023a). Moreover, Mehrgan et al. (2023a) probed for spatial variations of M/L and found very concentrated stellar M/L gradients on sub-kpc scales. We compare these new dynamical M/L inside the radius r_{main} (cf. Mehrgan et al. 2023a) where the mass decomposition between stellar and dark matter is very robust and average the dynamical gradients over the size of the radial bins used here.

M87: Our results from Voronoi bins are shown as filled blue symbols in Fig. 10, while open blue circles show the elliptical annuli.

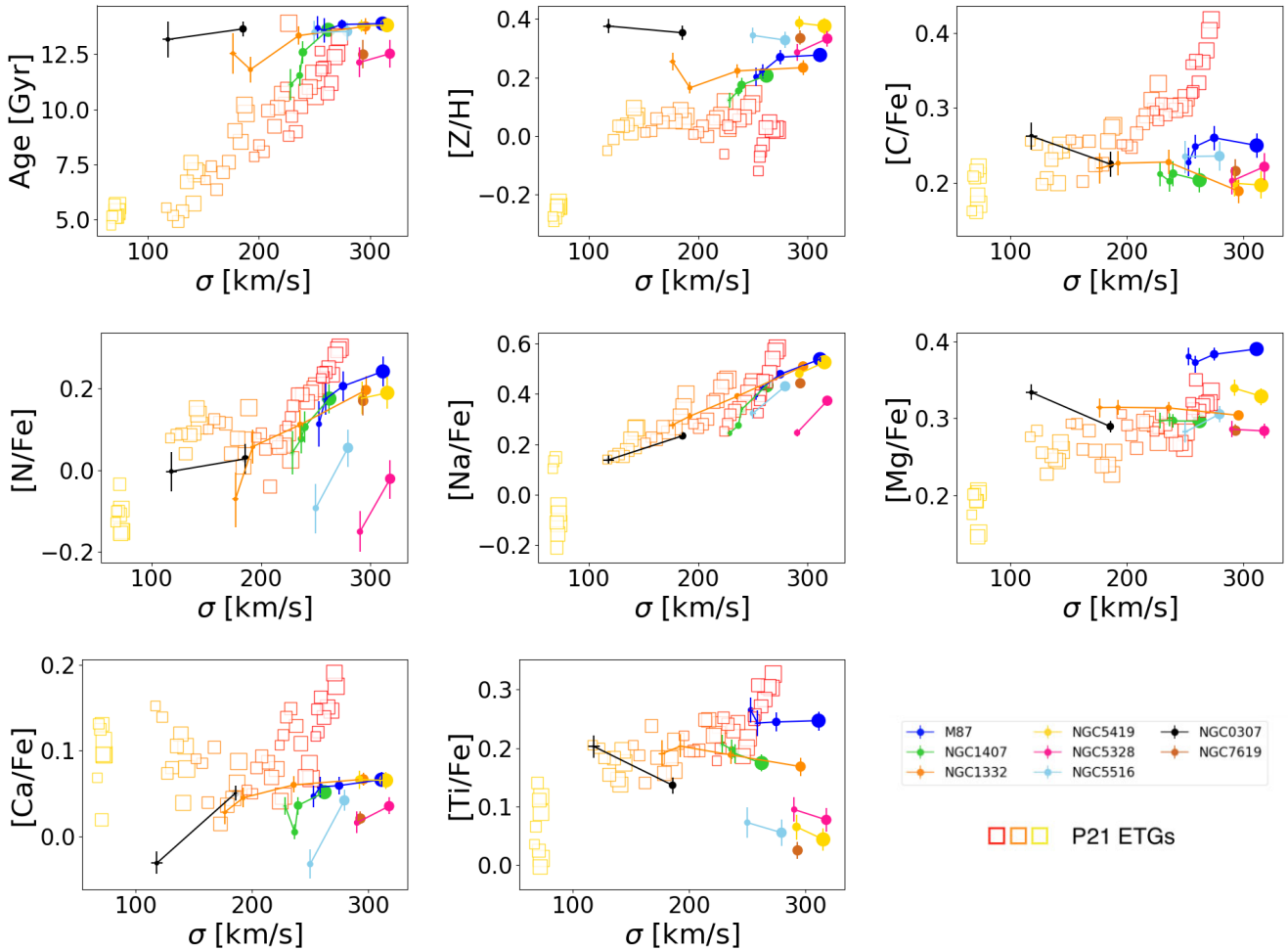


Figure 9. Stellar population parameters are shown against the local velocity dispersion for all galaxies. Square symbols show the results from P21 based on MaNGA data for early-type galaxies in six mass bins. Decreasing symbol size represents increasing radius, as before. The present galaxies correspond to the highest mass bin (red) from MaNGA or are even more massive. The galaxies in the present analysis are older and more metal-rich, but have shallower gradients. There are differences in the abundances of C, Ca, Ti possibly due to the treatment of these elements in the respective stellar population models and the available wavelength range.

Stellar population results from Sarzi et al. (2018) (red) are based on a different set of models which could explain their larger M/L . The shaded region for Sarzi et al. (2018) includes systematics due to the method of IMF determination. They made a comparison with the dynamical models from Oldham & Auger (2018) (yellow) and noted that the stellar population M/L were systematically larger. We find smaller M/L values, 5.5–7.5 in the centre and 4.5–5 at $0.4 R_e$, eliminating this systematic shift from the dynamical models.

Dynamical models with constant M/L are also shown from Gebhardt & Thomas (2009) (grey region) and Cappellari et al. (2006) (green line). These results are based on Schwarzschild and Jeans Anisotropic Modelling respectively, as well as different aperture sizes, which could be the reason for the difference. The three analyses that allow for a varying M/L with radius find remarkably similar gradients, which is a very encouraging result.

NGC 1407 and NGC 1332: Moving on to Fig. 11, we show our results for the other two galaxies from Voronoi bins (filled circles), radial bins (open symbols with lines). Our results for NGC 1407 agree with van Dokkum et al. (2017) (red), but they find a steeper

radial gradient. We use the same stellar population models and fitting procedure but their data is from the Low Resolution Imaging Spectrometer (LRIS) on the Keck I telescope, and includes the Wing-Ford band at 9920 \AA in the spectral range. However, this region of the spectrum is not fit very well and shows the largest residuals (see their figure 9). Their data also include C and Ca absorption features at bluer wavelengths up to 4000 \AA , however we find only mild differences (0.05 dex) between our abundance values. Also shown are dynamical models from Mehrgan et al. (2023a).

We find large central M/L for the fast rotator NGC 1332, and a flattening in the outer parts like NGC 1407. Dynamics are systematically below stellar populations and closer to the Kroupa level (shown in orange).

NGC 5419, NGC 307, NGC 5328, NGC 5516: We find M/L gradients in these galaxies as shown by the results from the radial bins. The stellar populations always give systematically larger M/L than dynamics. While Mehrgan et al. (2023a) also report M/L that increase towards the centre, the scale of these gradients is mostly within our central bin and the average of dynamics is closer to Kroupa (see also the discussion in Mehrgan et al. 2023a). The result from

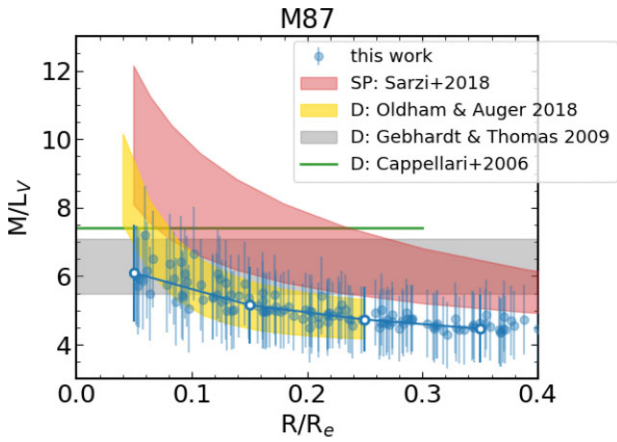


Figure 10. Comparison of our M/L (blue symbols) with results from literature for M87, where SP denotes stellar populations-based analyses and D denotes dynamical analyses. Results from our Voronoi binned data are shown as filled blue circles, while the radial bins are shown as open circles connected by lines. Sarzi et al. (2018) values (red) from fitting indices using a different set of stellar population models are systematically larger than our results by ~ 50 per cent. Our results have excellent agreement with the dynamical models of Oldham & Auger (2018) (yellow). Results from other dynamical models with a constant M/L (Gebhardt & Thomas 2009, grey; Cappellari et al. 2006, green) have similar values, differences are due to aperture sizes and different modelling techniques. This also highlights the importance of including M/L gradients in dynamical models to allow consistent comparisons.

triaxial dynamical modelling by Neureiter et al. (2023b) is shown for NGC 5419 as the red shaded region.

NGC 7619: For this galaxy we only analysed one average spectrum out to $0.2 R_e$, with $M/L = 7.1 \pm 1.5$. The models of Mehrgan et al. (2023a) yield 5.3 ± 1.4 over the same spatial scale, again systematically lower.

During our analysis we explored various sources of systematic errors. Possible systematics in the stellar population results could arise due to the models, including incompleteness of the underlying stellar library, and the assumed shape of the IMF. We discuss each of these in the following sections. For the dynamical models, uncertainties in M/L can arise from systematics in the dark matter halo models or from assumptions about axisymmetry (Thomas et al. 2007; Rusli et al. 2013; de Nicola et al. 2022; Neureiter et al. 2023a).

4.3 Models

Updated stellar population models described in Maraston et al. (2020) based on the MaStar stellar library (Yan et al. 2018) vastly expand on the available stellar parameter space. Low-mass dwarf stars are not well represented in other stellar libraries and are either included using a theoretical approach or via extrapolation. The new stellar library contains such stars very close to the hydrogen burning limit for the first time. Fig. 16 in Maraston et al. (2020) shows that for stellar population models based on these stars, the NaI absorption is much stronger in comparison to other widely used models. This would lead to shallower IMFs and smaller M/L . Fig. 13 shows that the difference between dynamics and stellar populations indeed increases with NaI. The Spearman correlation coefficient for this trend is $r_s = 0.86$ with a significance level of $p = 0.014$ indicating a strong correlation. Calibration of the NaI absorption might therefore be a significant source of systematics between dynamics and stellar populations. A potential correlation with the abundance-

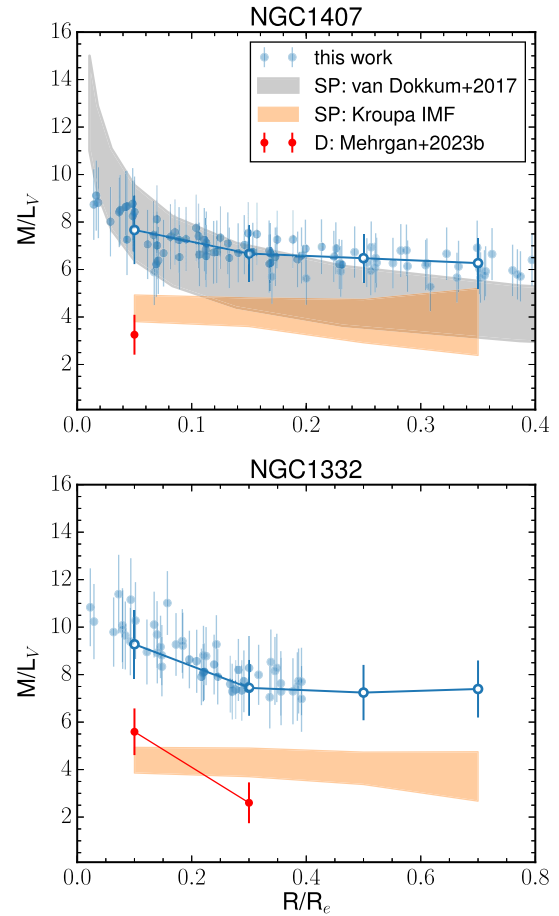


Figure 11. Comparison of M/L for NGC 1407 and NGC 1332 with literature, where SP denotes stellar populations-based analyses and D denotes dynamical analyses. Our results are shown in blue for different binning schemes: Voronoi bins (filled circles), radial bins (open circles connected by lines). Our NGC 1407 results agree well in the centre with van Dokkum et al. (2017) which are based on different data but same method and models. For both galaxies, dynamical M/L are shown in red. We focus on spatial scales where dark-matter does not affect the stellar M/L which restricts the comparison to the innermost radial bin for most galaxies. In general, stellar population results and dynamics agree in M/L that increase towards the centre. However, dynamical gradients are confined to sub-kpc scales (Mehrgan et al. 2023a) and are not resolved by the binning scheme used here. The bin-averaged M/L from dynamics are closer to Kroupa (orange shaded regions) than stellar populations.

sensitive NaD is weaker ($r_s = 0.71$ with $p = 0.07$). We suggest that a combination of correlated errors and the calibration of the NaI absorption is causing the systematics between dynamics and stellar populations.

4.4 IMF parametrization

Results also depend on the assumed shape of the IMF. Fig. 14 shows the derived IMF slope as a function of stellar mass for our sample of galaxies. The physical reason why the IMF slope would change from 2.3 above $1 M_\odot$ to values of 3 at intermediate masses, and falling again below a Salpeter slope at the lowest masses, is unclear.

We repeated our fits while fixing the IMF slope above $0.5 M_\odot$, X2, to the Salpeter value, and keeping the slope between 0.08 and $0.5 M_\odot$, X1, free. This parametrization was also used in our previous

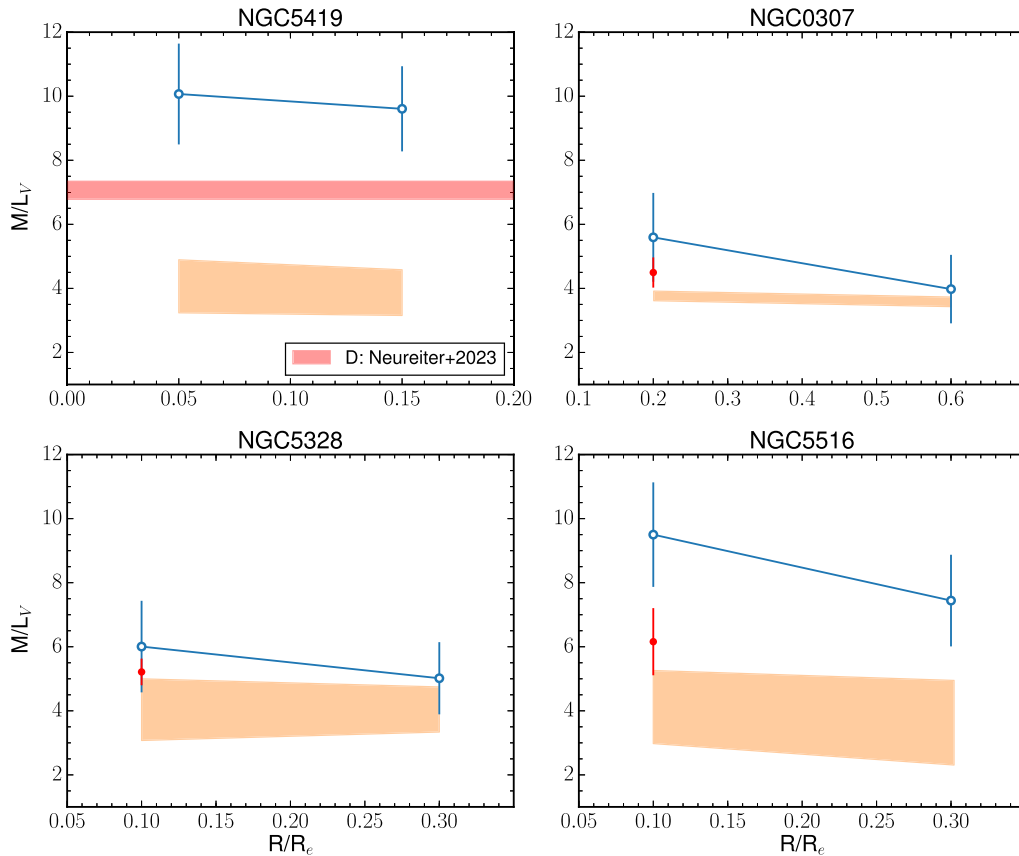


Figure 12. Comparison of our M/L (blue) with dynamical models (red) for the other four galaxies. These have been analysed in radial bins, shown as open circles. M/L from dynamics are systematically lower than from stellar populations. Except for NGC5419 they are close to the prediction for a Kroupa IMF (shown as orange shaded regions).

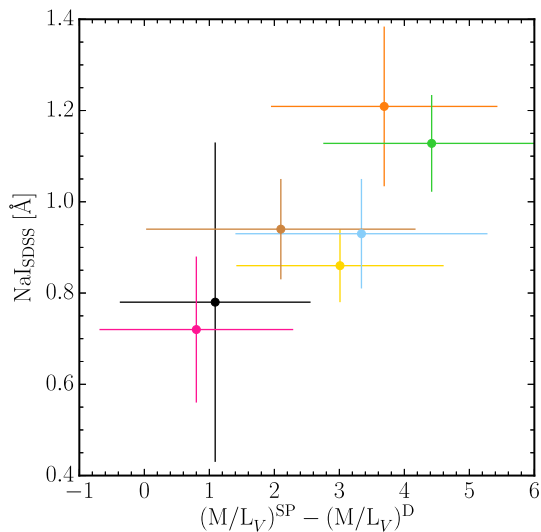


Figure 13. Difference between dynamics and stellar populations versus the NaI absorption strength. The stronger the NaI index, the more the stellar populations are biased high compared to dynamics, suggesting possible calibration issues of this line in combination with correlated uncertainties.

work (P18). With X2 fixed to 2.3, we found that X1 increased to large values, leading to an overall increase in M/L . E.g. for NGC 1407 we derived $M/L_V = 9.8 \pm 1.3$ and 8.2 ± 1.4 for the inner and outermost bins respectively, larger than both the van Dokkum et al. (2017) results as well as the dynamics.

Newman et al. (2017) explore a varying low-mass cutoff and find better agreement when the cutoff is larger at $0.15 M_\odot$, or by using non-parametric models with a turnover below $0.3 M_\odot$. We do not have access to non-parametric models but it would be important to test what happens when making no assumptions about the IMF shape.

5 CONCLUSIONS

We analysed the detailed stellar populations of a sample of eight massive early-type galaxies using MUSE data. Using full spectrum fitting we derived ages, metallicities, element abundances, IMF slopes, and M/L on high S/N binned spectra. Our conclusions are as follows:

- (i) The galaxies host old ages and negative metallicity gradients. They are all $[Mg/Fe]$ enhanced to at least twice solar values, with M87 most enhanced at $+0.4$ dex. We also present abundances of C, N, Na, Ca, and Ti, and compare these with literature.
- (ii) There is a range in IMF low-mass slope X1, with radial gradients, while X2 has high values ~ 3 at all radii. This leads to excess mass compared to a Kroupa IMF, with α_{Kroupa} between 1.5 and 2.5 for galaxy centres. We find no trend with kinematic morphology, a larger sample is needed to explore this in detail.

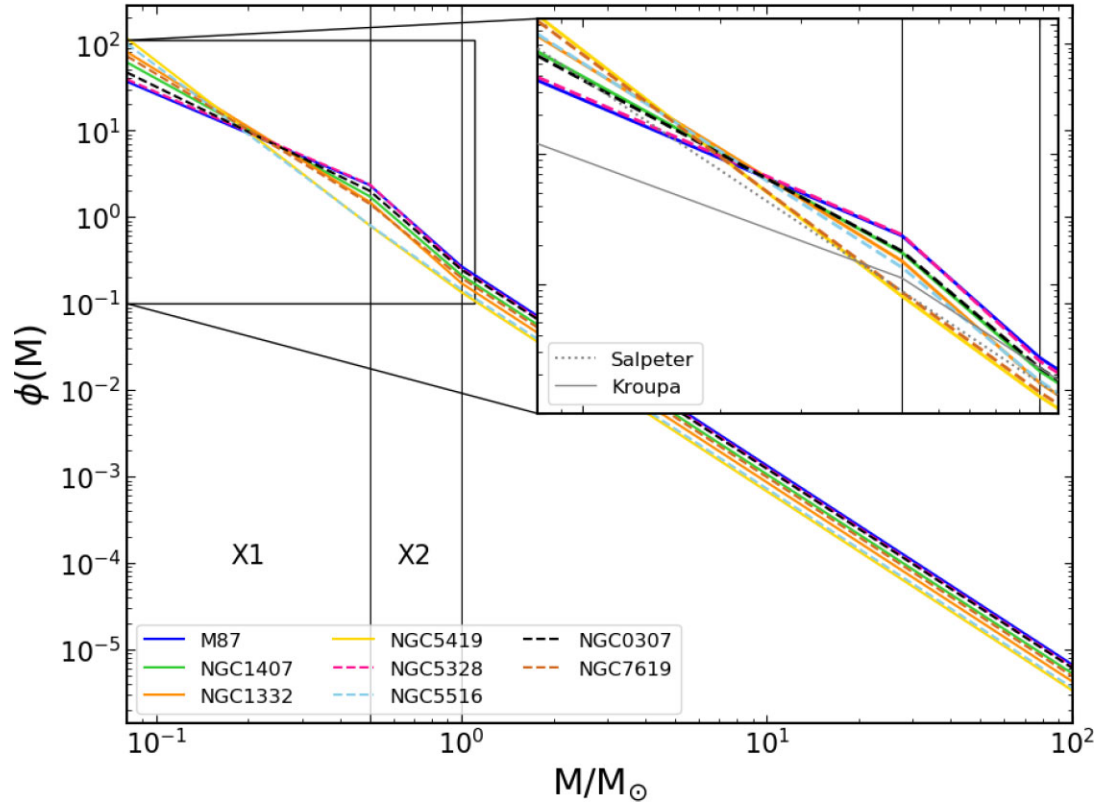


Figure 14. The IMF shape as derived for our galaxy sample is shown. X1 and X2 are free parameters, while the slope above $1 M_{\odot}$ is always fixed to 2.3. The inset zooms in on the low mass end, Kroupa and Salpeter IMFs are shown for reference. All IMFs are normalized to have the same mass. X1 clearly shows more variation among the galaxies.

(iii) M/L gradients from stellar populations and dynamics show excellent agreement for M87. We derive smaller M/L than stellar population results from literature based on different models. Meanwhile updated models with missing dwarf stars could lead to M/L smaller than our results, highlighting the uncertainty due to the stellar population synthesis and underlying stellar library.

(iv) For the other galaxies we compare to state-of-the-art orbit-based dynamical M/L with gradients and find stellar populations systematically higher than dynamics. The discrepancy increases systematically with the NaI absorption strength, suggesting that improved calibration of the NaI absorption could be the key to reconciling dynamics and stellar populations.

(v) There is strong motivation for measuring dynamical stellar M/L gradients of individual galaxies as an independent comparison with stellar population-based results to test models and identify sources of systematics.

ACKNOWLEDGEMENTS

We thank Daniel Thomas for fruitful discussions. Computations were performed on the high performance computing (HPC) resources of the Max Planck Computing and Data Facility in Garching, and the Sciamia HPC cluster which was supported by the Institute of Cosmology of Gravitation, SEPnet, and the University of Portsmouth. TP acknowledges Development Projects Funding from the University of Portsmouth. This research made use of the PYTHON packages NUMPY (Walt, Colbert & Varoquaux 2011), SCIPY (Jones et al. 2001), MATPLOTLIB (Hunter 2007), and ASTROPY (Astropy Collaboration 2013).

DATA AVAILABILITY

Data generated by the analysis in this work are available upon reasonable request from the corresponding authors.

REFERENCES

- Astropy Collaboration 2013, *A&A*, 558, A33
 Barber C., Schaye J., Crain R. A., 2019, *MNRAS*, 483, 985
 Bender R., Burstein D., Faber S. M., 1992, *ApJ*, 399, 462
 Bernardi M. et al., 2018, *MNRAS*, 475, 757
 Bernardi M., Domínguez Sánchez H., Brownstein J. R., Drory N., Sheth R. K., 2019, *MNRAS*, 489, 5633
 Cappellari M., 2017, *MNRAS*, 466, 798
 Cappellari M. et al., 2006, *MNRAS*, 366, 1126
 Cappellari M. et al., 2012, *Nature*, 484, 485
 Cappellari M. et al., 2013, *MNRAS*, 432, 1862
 Cenaro A. J., Gorgas J., Vazdekis A., Cardiel N., Peletier R. F., 2003, *MNRAS*, 339, 12
 Chabrier G., 2003, *PASP*, 115, 763
 Collett T. E. et al., 2018, *Science*, 360, 1342
 Collier W. P., Smith R. J., Lucey J. R., 2018, *MNRAS*, 478, 1595
 Conroy C., van Dokkum P., 2012a, *ApJ*, 747, 69
 Conroy C., van Dokkum P. G., 2012b, *ApJ*, 760, 71
 Conroy C., Villaume A., van Dokkum P. G., Lind K., 2018, *ApJ*, 854, 139
 Domínguez Sánchez H., Bernardi M., Brownstein J. R., Drory N., Sheth R. K., 2019, *MNRAS*, 489, 5612
 Emsellem E. et al., 2011, *MNRAS*, 414, 888
 Erwin P., Thomas J., Saglia R. P., Fabricius M., Rusli S. P., Seitz S., Bender R., 2018, *MNRAS*, 473, 2251
 Feldmeier-Krause A., Lonoce I., Freedman W. L., 2020, *ApJ*, 902, 12
 Gebhardt K., Thomas J., 2009, *ApJ*, 700, 1690

- Gu M., Greene J. E., Newman A. B., Kreisch C., Quenneville M. E., Ma C.-P., Blakeslee J. P., 2022, *ApJ*, 932, 103
- Guszejnov D., Hopkins P. F., Graus A. S., 2019, *MNRAS*, 485, 4852
- Hunter J. D., 2007, *Comput. Sci. Eng.*, 9, 90
- Johansson J., Thomas D., Maraston C., 2012, *MNRAS*, 421, 1908
- Jones E., Oliphant T., Peterson P. et al., 2001, SciPy: Open Source Scientific Tools for Python, Available at: <http://www.scipy.org/>
- Kormendy J., Fisher D. B., Cornell M. E., Bender R., 2009, *ApJS*, 182, 216
- Kroupa P., 2001, *MNRAS*, 322, 231
- La Barbera F., Ferreras I., Vazdekis A., de la Rosa I. G., de Carvalho R. R., Trevisan M., Falcón-Barroso J., Ricciardelli E., 2013, *MNRAS*, 433, 3017
- La Barbera F. et al., 2019, *MNRAS*, 489, 4090
- Lauer T. R., 2012, *ApJ*, 759, 64
- Li H. et al., 2017, *ApJ*, 838, 77
- Lipka M., Thomas J., 2021, *MNRAS*, 504, 4599
- Lyubenova M. et al., 2016, *MNRAS*, 463, 3220
- Mann A. W., Feiden G. A., Gaidos E., Boyajian T., von Braun K., 2015, *ApJ*, 804, 64
- Maraston C. et al., 2020, *MNRAS*, 496, 2962
- Martín-Navarro I., La Barbera F., Vazdekis A., Falcón-Barroso J., Ferreras I., 2015a, *MNRAS*, 447, 1033
- Martín-Navarro I. et al., 2015b, *ApJ*, 806, L31
- Martín-Navarro I. et al., 2021, *A&A*, 654, A59
- Mazzalay X., Thomas J., Saglia R. P., Wegner G. A., Bender R., Erwin P., Fabricius M. H., Rusli S. P., 2016, *MNRAS*, 462, 2847
- Mehrgan K., Thomas J., Saglia R., Parikh T., Neureiter B., Erwin P., Bender R., 2023a, *MNRAS*, 000, 1
- Mehrgan K., Thomas J., Saglia R., Parikh T., Bender R., 2023b, *ApJ*, 948, 79
- Neureiter B., de Nicola S., Thomas J., Saglia R., Bender R., Rantala A., 2023a, *MNRAS*, 519, 2004
- Neureiter B., Thomas J., Rantala A., Naab T., Mehrgan K., Saglia R., de Nicola S., Bender R., 2023b, *ApJ*, 950, 15
- Newman A. B., Smith R. J., Conroy C., Villaume A., van Dokkum P., 2017, *ApJ*, 845, 157
- de Nicola S., Neureiter B., Thomas J., Saglia R. P., Bender R., 2022, *MNRAS*, 517, 3445
- Oldham L., Auger M., 2018, *MNRAS*, 474, 4169
- Parikh T. et al., 2018, *MNRAS*, 477, 3954 (P18)
- Parikh T. et al., 2019, *MNRAS*, 483, 3420
- Parikh T., Thomas D., Maraston C., Westfall K. B., Andrews B. H., Boardman N. F., Drory N., Oyarzun G., 2021, *MNRAS*, 502, 5508
- Poci A. et al., 2022, *MNRAS*, 514, 3660
- Rusli S. P., Thomas J., Erwin P., Saglia R. P., Nowak N., Bender R., 2011, *MNRAS*, 410, 1223
- Rusli S. P. et al., 2013, *AJ*, 146, 45
- Saglia R. P., Maraston C., Thomas D., Bender R., Colless M., 2002, *ApJ*, 579, L13
- Salpeter E. E., 1955, *ApJ*, 121, 161
- Sarzi M., Spiniello C., La Barbera F., Krajnović D., van den Bosch R., 2018, *MNRAS*, 478, 4084
- Smith R. J., 2014, *MNRAS*, 443, L69
- Smith R. J., 2020, *ARA&A*, 58, 577
- Thomas J., Lipka M., 2022, *MNRAS*, 514, 6203
- Thomas J., Jesseit R., Naab T., Saglia R. P., Burkert A., Bender R., 2007, *MNRAS*, 381, 1672
- Thomas D., Maraston C., Johansson J., 2011a, *MNRAS*, 412, 2183
- Thomas J. et al., 2011b, *MNRAS*, 415, 545
- Trager S. C., Worthey G., Faber S. M., Burstein D., González J. J., 1998, *ApJS*, 116, 1
- van Dokkum P., Conroy C., Villaume A., Brodie J., Romanowsky A. J., 2017, *ApJ*, 841, 68
- Vazdekis A., Ricciardelli E., Cenarro A. J., Rivero-González J. G., Díaz-García L. A., Falcón-Barroso J., 2012, *MNRAS*, 424, 157
- Verro K. et al., 2022, *A&A*, 660, A34
- Villaume A., Conroy C., Johnson B., Rayner J., Mann A. W., van Dokkum P., 2017, *ApJS*, 230, 23
- Walt S. V. D., Colbert S. C., Varoquaux G., 2011, *Comput. Sci. Eng.*, 13, 22
- Worthey G., Faber S. M., Gonzalez J. J., Burstein D., 1994, *A&AS*, 94, 687
- Yan R. et al., 2018, *Nucl. Phys. B*, 586, 349

APPENDIX A: FITS

The best-fitting models to the inner and outermost radially binned spectra are shown for the other galaxies in our analysis in Figs. A1 – A7.

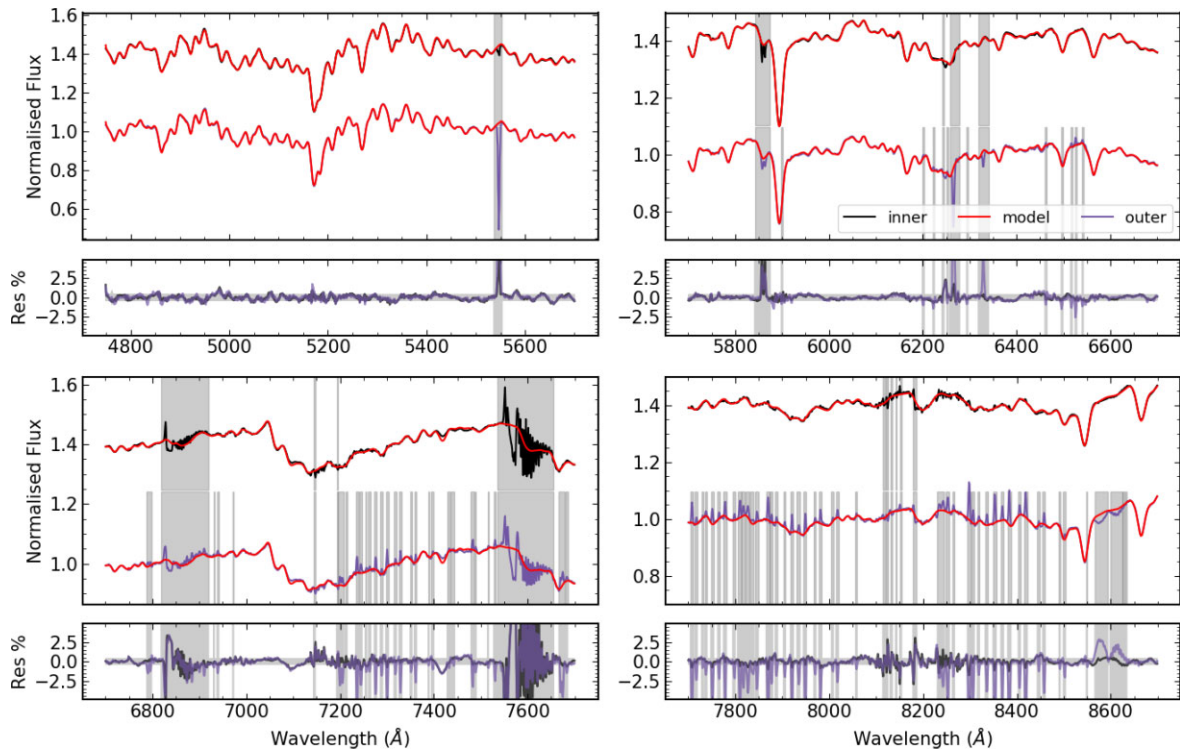


Figure A1. Stellar population model fit to the central and outermost radially binned spectrum of NGC 1407. Masked regions affected by sky lines and telluric absorption are shown in grey. Residuals between the data and model are shown in the bottom panels, and the horizontal grey band shows the error on the data.

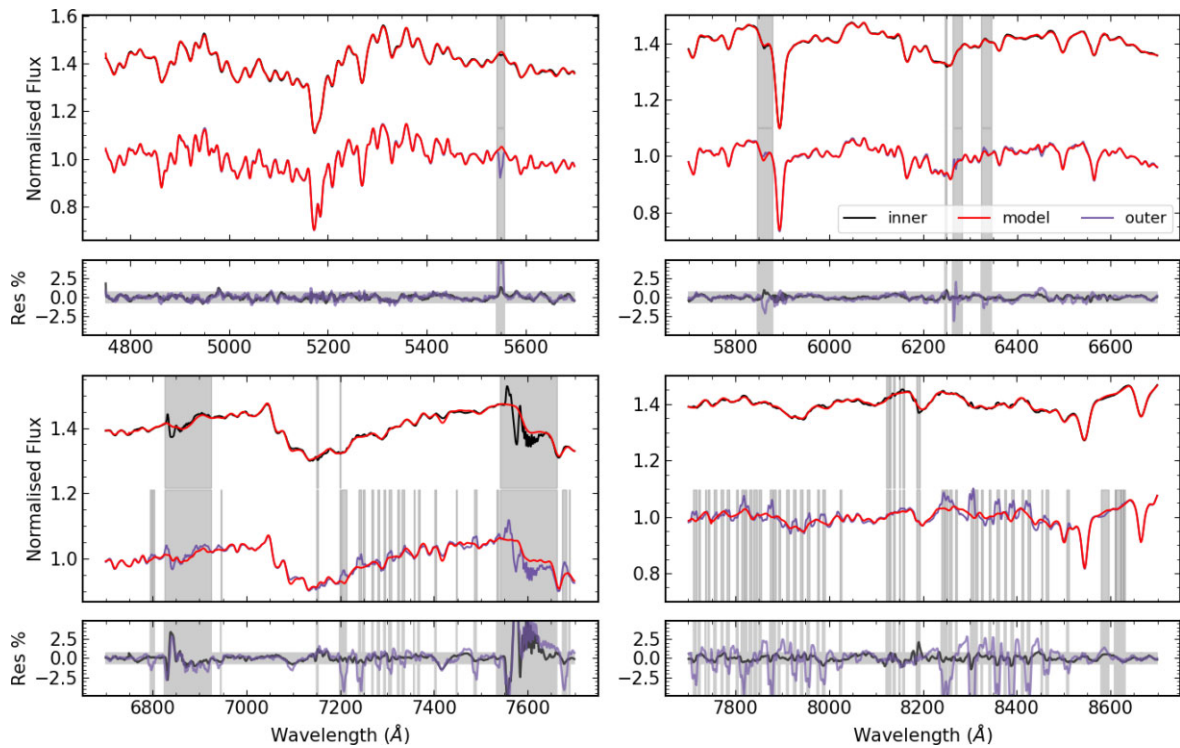


Figure A2. Same for NGC 1332.

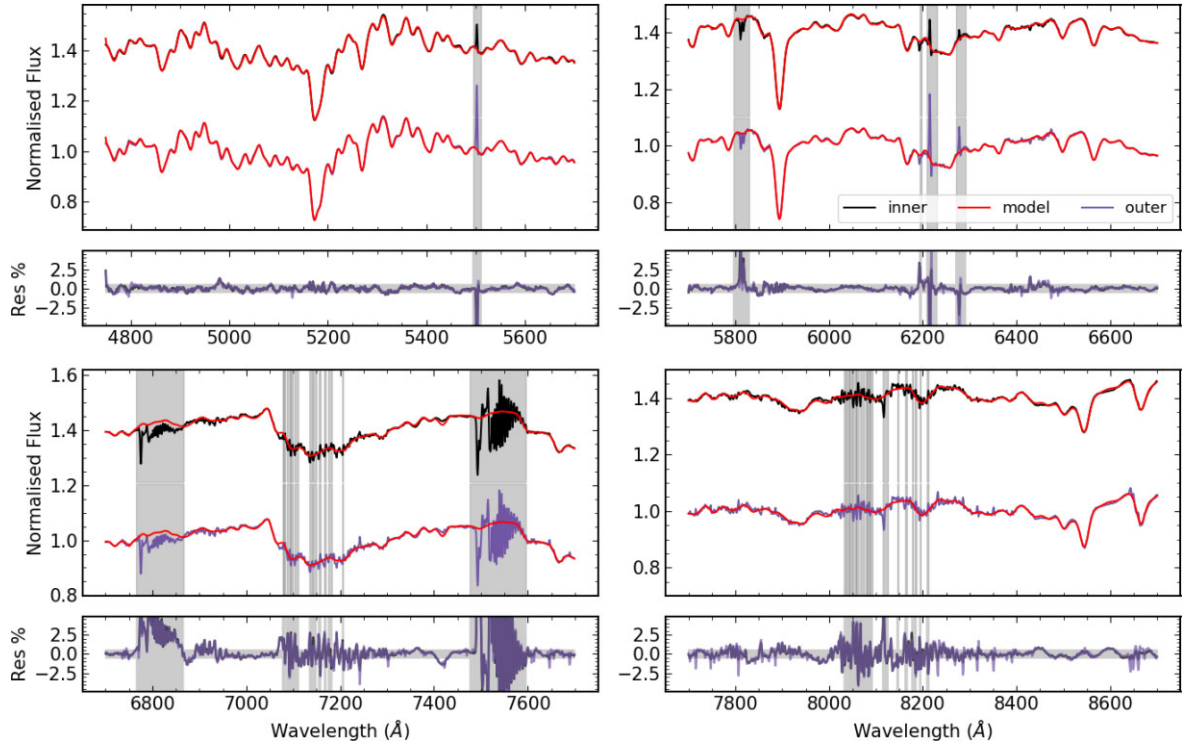


Figure A3. Same for NGC 5419.

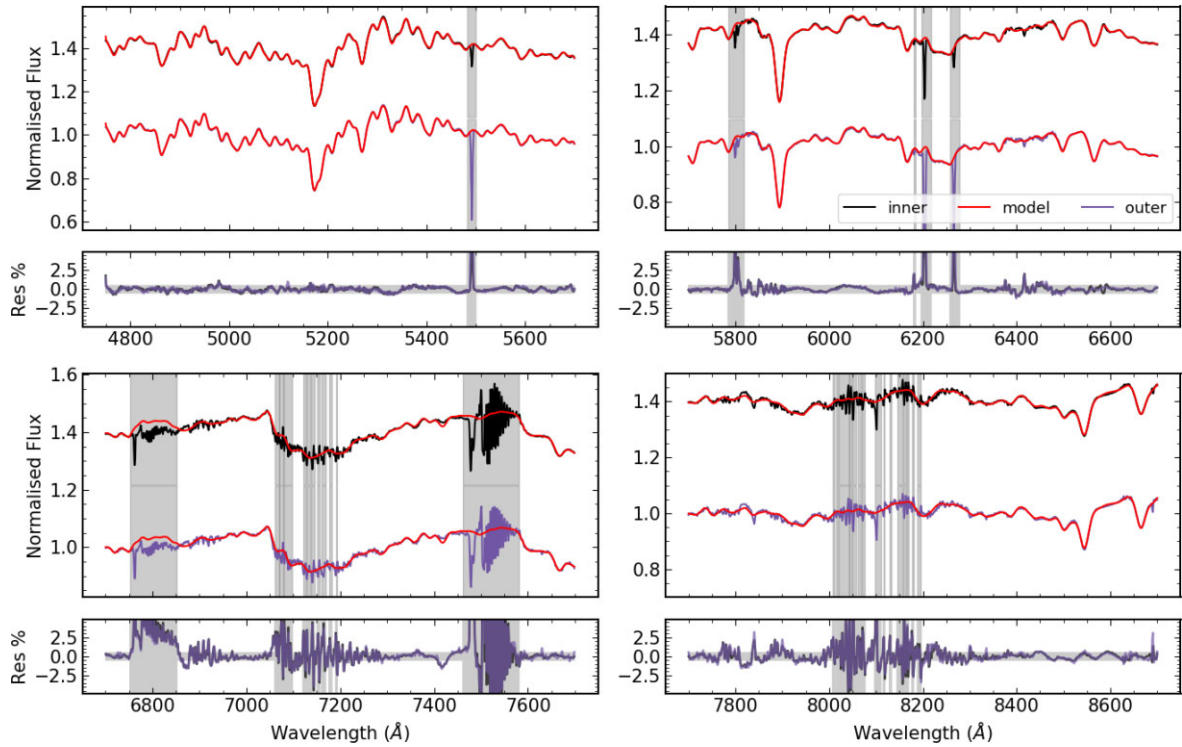


Figure A4. Same for NGC 5328.

Downloaded from https://academic.oup.com/mnras/article/528/4/7338/7608527 by Max Planck Institute for Astrophysics user on 11 March 2024

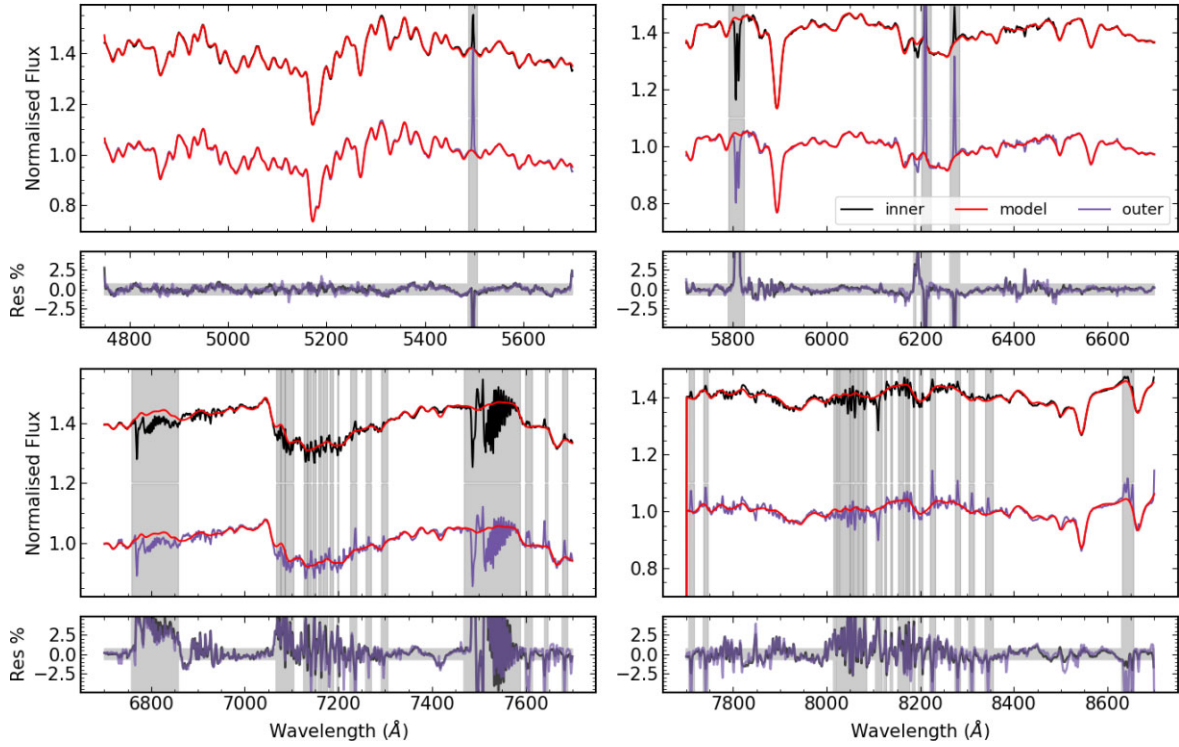


Figure A5. Same for NGC 5516.

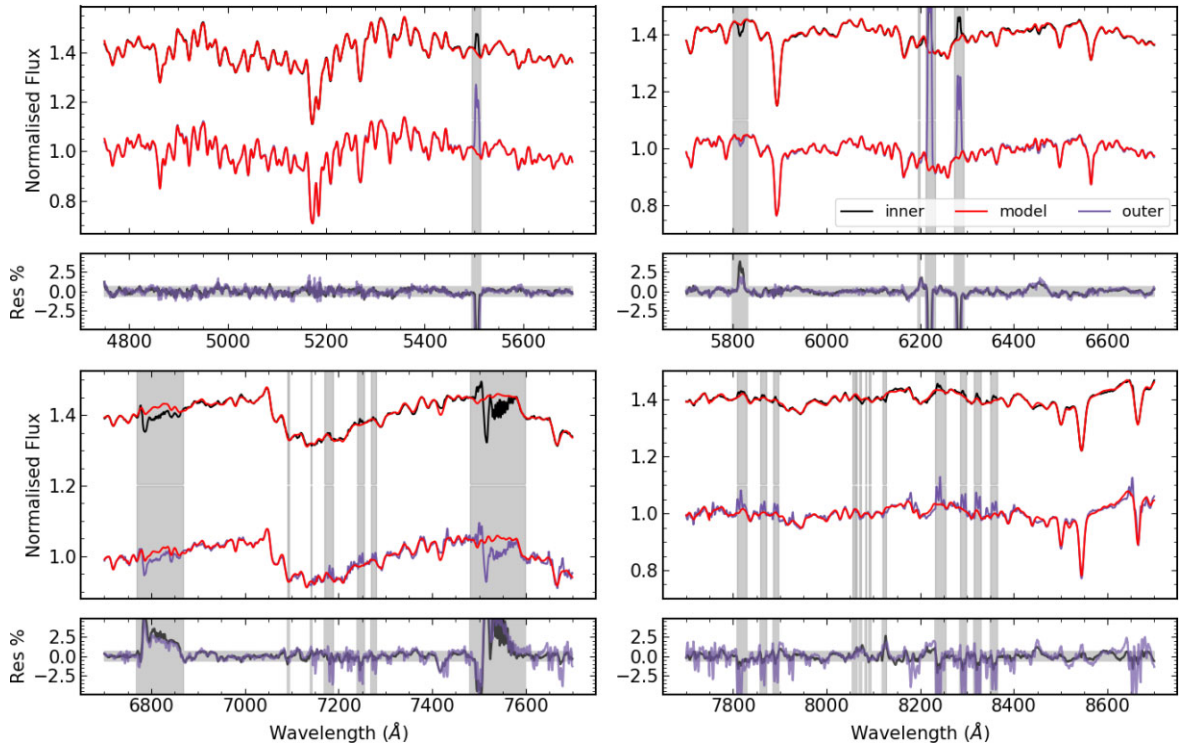


Figure A6. Same for NGC 307.

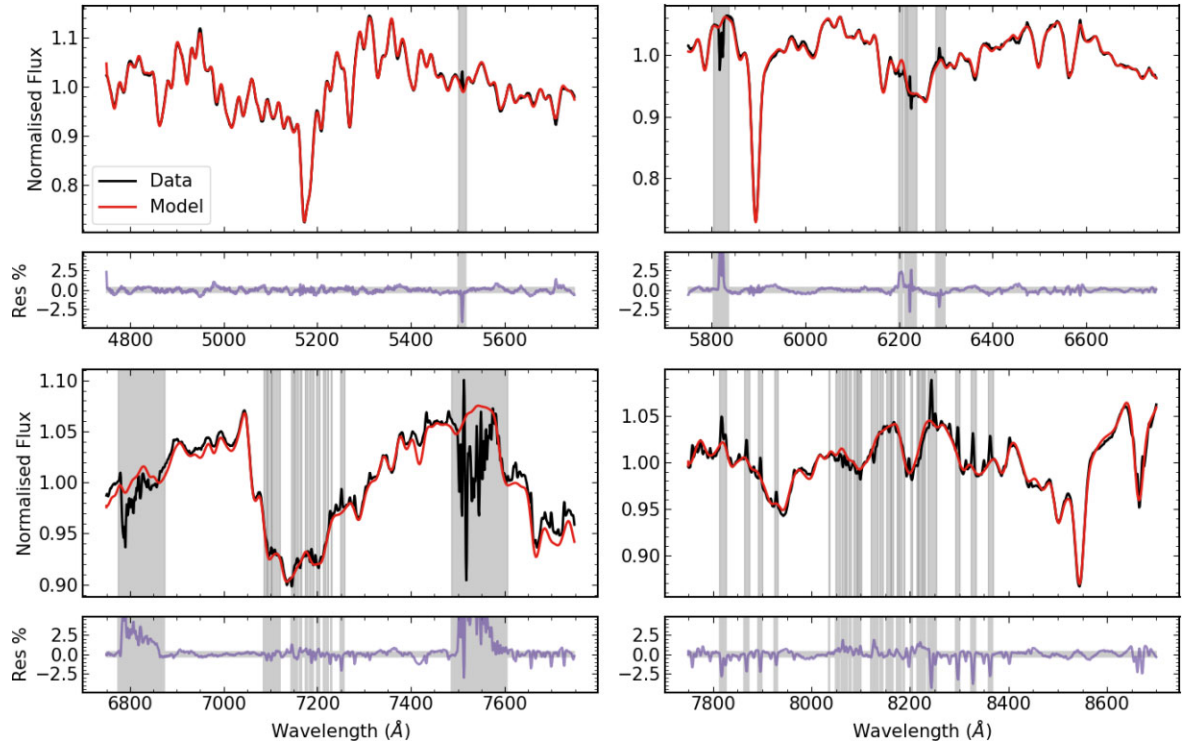


Figure A7. Same for NGC 7619.

APPENDIX B: MAPS

The stellar population parameters derived from full spectrum fitting are shown as maps in Figs. B1 & B2 for the remaining two galaxies in the detailed Voronoi binning scheme.

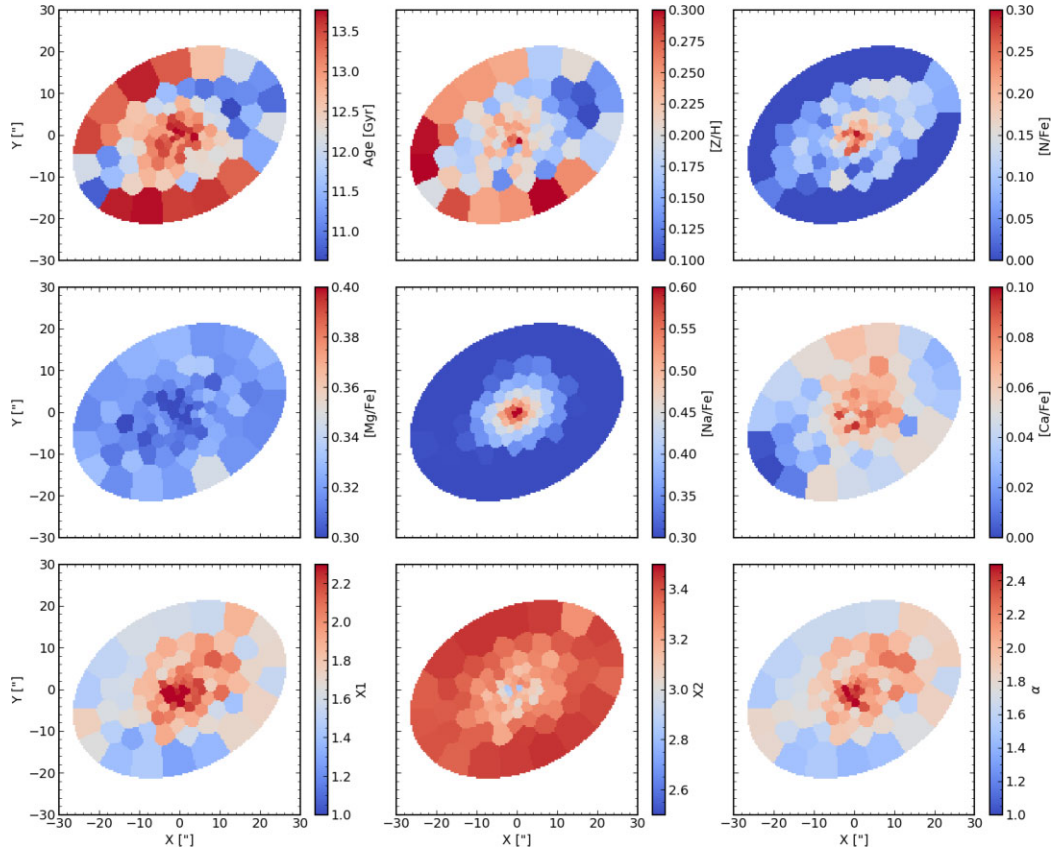


Figure B1. Stellar population maps for NGC 1332.

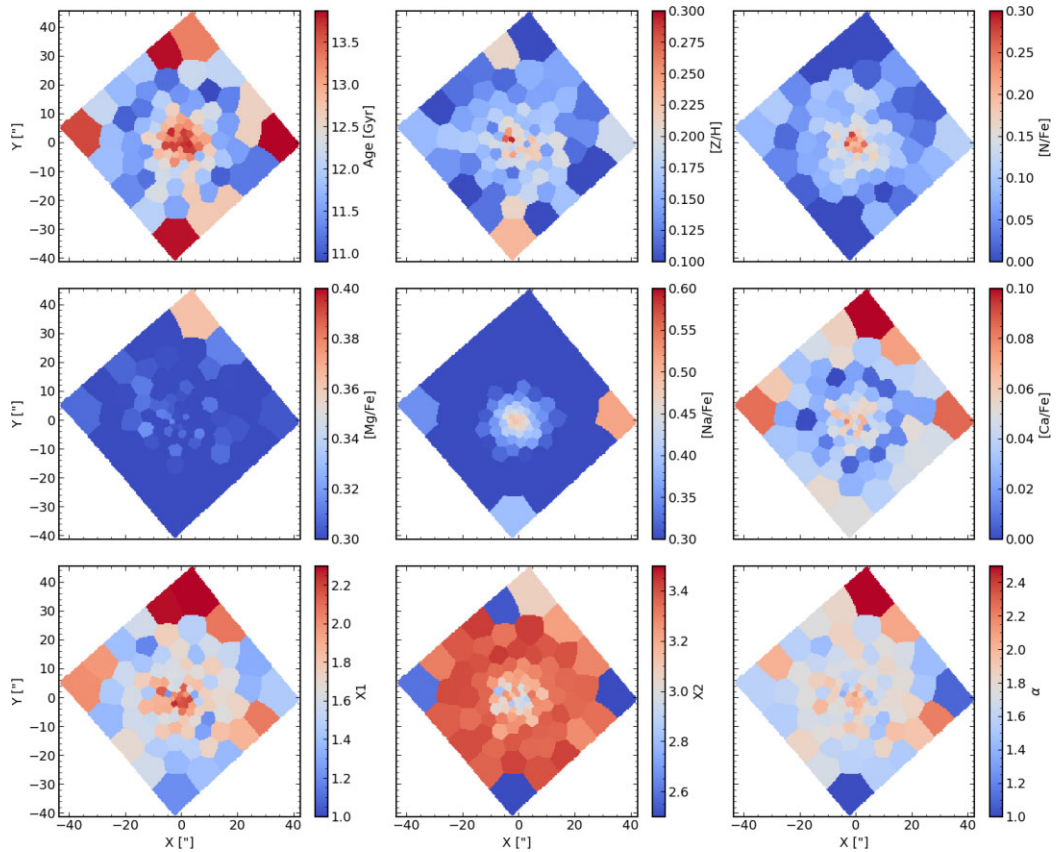


Figure B2. Stellar population maps for NGC 1407.

APPENDIX C: LOSVD SHAPE

We also derive higher order Gauss–Hermite moments, h_3 and h_4 , from the full spectrum fitting. For the Voronoi binned galaxies, we find maps fully consistent with Mehrgan et al. (2023b), giving confidence in the derived parameters from ALF. Generally the results show that LOSVD wings are stronger in galaxy centres and for FRs. Fig. C1 shows these parameters for the radial bins. Small h_3 and h_4 are measured in galaxy centres, suggesting that these LOSVDs are Gaussian, and hence unaffected by biased parameters. However at large radii, for fast rotators we see sharp rises in h_4 , e.g. NGC 1332 and NGC 307. This is because the galaxies have strong rotation in the outskirts, and averaging these spectra together distorts the LOSVD shape.

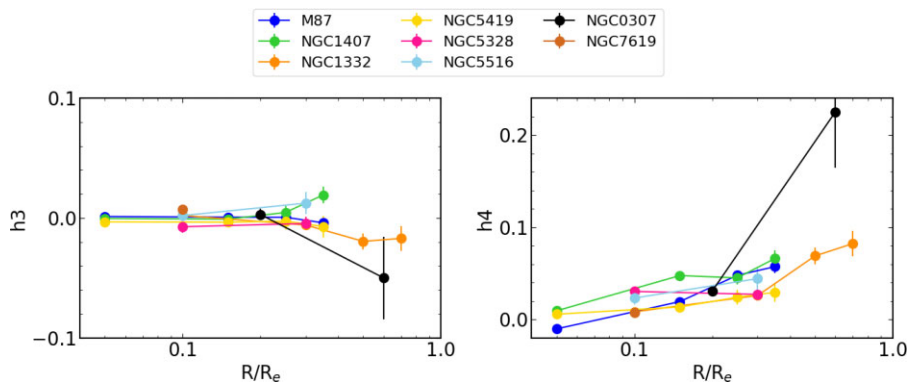


Figure C1. Higher order Gauss–Hermite moments, h_3 and h_4 , as a function of radius for radially binned spectra of all galaxies. The LOSVD appears to be Gaussian in galaxy centres, while h_4 rises at large radii for FRs (NGC 1332 and NGC 307), suggesting that the stellar population parameters are unaffected by biases due to the LOSVD shape apart from in these regions.

This paper has been typeset from a \LaTeX file prepared by the author.